Energy Materials

Review

Check for updates

Development of catalysts and reactor designs for CO$_2$ electroreduction towards C$_{2+}$ products

Joonhee Ma, Soo Young Kim[*] (ID)

Department of Materials Science and Engineering, Korea University, Seoul 02841, Republic of Korea.

[*]**Correspondence to:** Prof. Soo Young Kim, Department of Materials Science, Korea University, 145 Anam-ro, Seongbuk-gu, Seoul 02841, Republic of Korea. E-mail: sooyoungkim@korea.ac.kr

Abstract

Recent research on the electrocatalytic CO$_2$ reduction reaction (eCO$_2$RR) has garnered significant attention given its capability to address environmental issues associated with CO$_2$ emissions while harnessing clean energy to produce high-value-added products. Compared to C$_1$ products, C$_{2+}$ products provide greater energy densities and are highly sought after as chemical feedstocks. However, the formation of the C-C bond is challenging due to competition with the formation of H-H and C-H bonds. Therefore, to elevate the selectivity and yield of C$_{2+}$ fuels, it is essential to develop more advanced electrocatalysts and optimize the design of electrochemical cell configurations. Of the materials investigated for CO$_2$RR, Cu-based materials stand out due to their wide availability, affordability, and environmental compatibility. Moreover, Cu-based catalysts exhibit promising capabilities in CO$_2$ adsorption and activation, facilitating the formation of C$_{2+}$ compounds via C-C coupling. This review examines recent research on both electrocatalysts and electrochemical cells for CO$_2$ electroreduction to C$_{2+}$ compounds, introducing the core principles of eCO$_2$RR and the reaction pathways involved in generating C$_{2+}$ products. A key focus is the categorization of Cu-based catalyst designs, including defect engineering, surface modification, nanostructure engineering, and tandem catalysis. By analyzing recent studies on eCO$_2$RR with Cu-based catalysts, we aim to elucidate the mechanisms behind enhanced selectivity for C$_{2+}$ compounds. Additionally, various types of electrolytic cells are discussed. Lastly, the prospects and limitations of utilizing Cu-based materials and electrocatalytic cells for CO$_2$ reduction are highlighted for future research.

Keywords: CO$_2$ reduction, electrocatalysis, C$_{2+}$ products, Cu, electrocatalytic cells

INTRODUCTION

The significant release of CO_2 from the use of fossil fuels has brought about its accumulation in the atmosphere, disrupting the global carbon cycle and causing serious environmental and climate issues, including the greenhouse gas effect and rising sea levels[1-7]. Consequently, there is a growing interest in converting CO_2 into valuable carbon-based compounds to reduce atmospheric CO_2 concentrations and tackle energy challenges[8,9]. Various approaches have been investigated by researchers to transform CO_2 into valuable carbon-based compounds, including chemical conversion[10], biotransformation[11], photocatalysis[12,13], and electrocatalysis[14-16]. Among these approaches, the eCO_2RR stands out as a promising technique, leveraging renewable electricity to mitigate CO_2-related environmental problems while generating high-value-added products[17-19].

In aqueous electrolyte media, electrocatalytic CO_2 reduction reaction (eCO_2RR) products can be classified into two main categories: (i) $2e^-$ products, such as carbon monoxide (CO) and formate ($HCOO^-$), and (ii) multi-electron transfer products, including methanol (CH_3OH), methane (CH_4), ethanol (C_2H_5OH), and ethylene (C_2H_4)[20,21]. Compared to $2e^-$ products, multi-electron transfer products are preferred due to their higher economic value, serving as crucial feedstock and specialized chemicals [Figure 1A][22].

However, achieving selective CO_2 reduction into C_{2+} multi-carbon products remains challenging due to several factors: (1) the competitive and undesirable H_2O reduction, (2) the large C-C coupling activation barrier, and (3) the difference in overpotential for the formation of crucial CO intermediates and C_{2+} species, resulting in lower current densities and selectivity compared to C_1 products [Figure 1B and C][23-27]. Therefore, developing advanced electrocatalysts is essential for enhancing both the selectivity and activity for C_{2+} production[28,29].

This review provides a detailed examination of strategies designed to control C-C coupling and multi-electron transfer product processes, specifically focusing on promising electrocatalysts for eCO_2RR that produce C_{2+} compounds. We first introduce the fundamentals of electrocatalytic CO_2 reduction, discussing the mechanisms and possible reaction pathways for converting CO_2 into C_{2+} compounds. Various approaches to optimize the selectivity of Cu-based electrocatalysts for C_{2+} production are then explored. Additionally, recent advancements in electrochemical cell design for CO_2 reduction are reviewed. The paper concludes by highlighting the primary challenges that remain and offering future insights into the development of Cu-based catalysts and electrochemical cells for CO_2-to-C_{2+} conversion.

FUNDAMENTAL INSIGHTS INTO CO_2 REDUCTION REACTION MECHANISMS

CO_2 is a highly stable molecule, primarily due to its strong C=O bond, which has a bond dissociation energy of 750 kJ mol^{-1}[30]. Converting CO_2 into desired products requires very challenging conditions and substantial energy input. This transformation involves multi-electron transfer steps, such as 2-, 4-, 6-, 8-, or even 18-electron processes, resulting in a range of possible products [Figure 2][31].

These products can be categorized into two groups according to the quantity of carbon atoms: C_1 products, including CO, CH_4, HCOOH, and CH_3OH; C_2 products, including acetate, C_2H_4, and C_2H_5OH; C_3 products, including propanol (C_3H_7OH) and acetone (CH_3COCH_3); and C_{4+} products[32]. Table 1 summarizes the thermodynamic half-reaction of CO_2 conversion and the associated standard potential to produce specific products[33]. The reaction mechanism for eCO_2RR involves several key steps: CO_2 adsorption onto the catalyst surface, electron and proton transfer, the formation of reactive intermediates, and the desorption of the final products. The performance and selectivity of this process are heavily dependent on factors such as the choice of catalyst material, the composition of the electrolyte, and the applied potential[34]. A critical
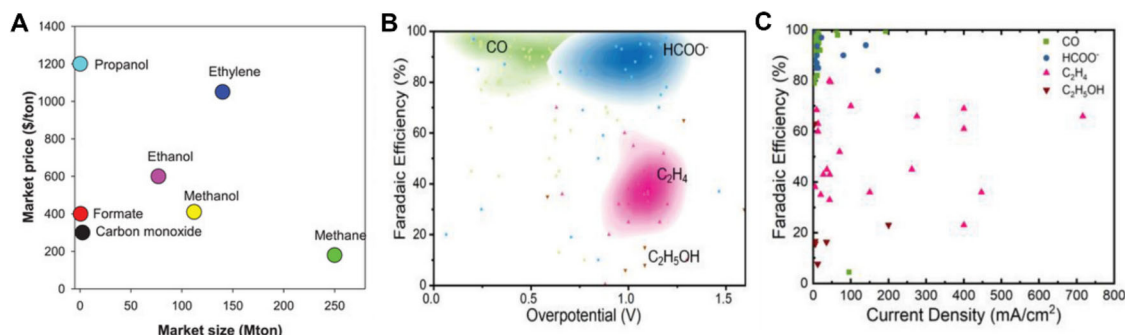
Figure 1. (A) Market size and price of CO_2RR products; (B) Faradaic efficiency and corresponding overpotential; (C) Maximum faradaic efficiency and current density. This figure is quoted with permission from Kibria *et al.* Copyright (2019) John Wiley and Sons[22]. CO_2RR: CO_2 reduction reaction.
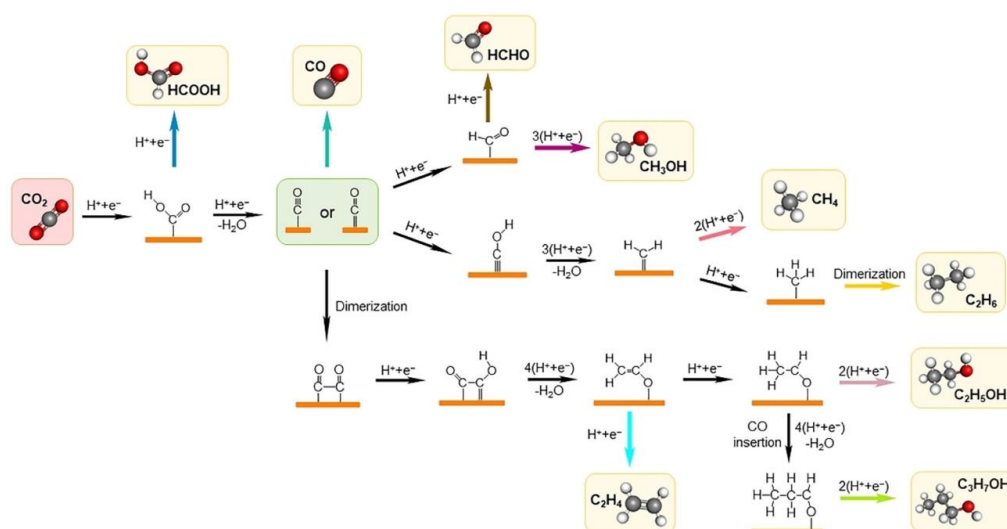

Figure 2. Overview of the reaction routes of CO_2RR for both C_1 and C_{2+} products. This figure is quoted with permission from Trogadas *et al.* Copyright (2023) John Wiley and Sons[31]. CO_2RR: CO_2 reduction reaction.

aspect of determining reaction pathways and product distributions lies in understanding the binding energies of intermediates on the catalyst surface. Additionally, operating conditions, including the pH and temperature of the electrolyte, play a significant role in influencing reaction dynamics and product selectivity.

MECHANISM FOR C_{2+} PRODUCTS

C_{2+} products typically possess higher energy densities than C_1 products, making them essential feedstocks in numerous chemical industries [33]. Consequently, the CO_2 reduction reaction (CO_2RR) into valuable C_{2+} products is highly desirable. A critical step in achieving multi-carbon products during CO_2RR is the coupling of two C_1 intermediates to form a C-C bond. The *CO intermediate plays a pivotal role in this process: it can either undergo C-C coupling with another *CO species to produce C_{2+} products, such as ethanol, ethylene, and n-propanol, or it can strongly adsorb on the catalyst surface and proceed through hydrogenation to form C_1 products such as CH_4.[35] However, the selective generation of C_{2+} products faces substantial challenges. First of all, a C-C coupling process requires significant energy barriers, and the formation of C_{2+} products involves multiple proton-electron transfer steps, which are inherently slow and

kinetically hindered[36-39]. In contrast, competing reactions involving H-H and C-H bond formation occur more readily due to their lower energy barriers and simpler reaction pathways[40-42]. These results in decreased activity and selectivity for C_{2+} product formation during CO_2 reduction. Generally, the process of C_{2+} product formation involves four key steps: (1) ˙CO formation; (2) C-C bond formation; (3) C-C coupling; and (4) product desorption[43]. An important aspect of generating C_{2+} products is maintaining a substantial amount of ˙CO on the surface, as a higher concentration of CO promotes C-C coupling, thereby boosting the production of C_{2+} compounds. The C-C bond formation in CO_2 reduction can occur via two distinct mechanisms: the Eley-Rideal (E-R) and the Langmuir-Hinshelwood (L-H) mechanisms[24]. In the E-R mechanism, a CO molecule from the gas phase interacts directly with CO species already adsorbed on the catalyst surface, facilitating C-C coupling[44]. This pathway typically arises when one reactant remains in the gas phase while the other is adsorbed on the surface. Conversely, the L-H mechanism involves the adsorption of both CO molecules onto the catalyst surface, where they subsequently interact to form C-C bonds[45]. This process becomes predominant when the catalyst surface is sufficiently populated with adsorbed CO, allowing interactions between these species. A comprehensive understanding of the dynamic interplay between these two mechanisms is key to advancing the selective formation of C_{2+} products in CO_2 reduction processes. Additionally, the selectivity and reaction pathways for C_{2+} formation are strongly influenced by the properties of Cu-based electrocatalysts and the electrolyte environment[46,47]. Thus, it is imperative to develop an ideal catalyst that suppresses the hydrogen evolution reaction (HER) while featuring minimal energy barriers for CO_2 activation and C-C bond formation[48-50].

CATALYST DESIGN FOR PROMOTING THE REACTION PATHWAY FOR C_{2+} PRODUCTS

To date, Copper (Cu) stands out as one of the rare metal catalysts capable of efficiently converting CO_2 into valuable multi-carbon products[51]. This is attributed to its distinctive 3d electronic structure, which provides optimal *CO binding energy and suppresses HER activity, thereby promoting C-C coupling[52]. Furthermore, Cu-based catalysts stand out as the most promising option for CO_2 reduction to C_{2+} products, offering an optimal balance of environmental sustainability, economic feasibility, and superior selectivity. While alternative catalysts may offer lower costs, none rival the unique ability of Cu to facilitate the production of high-value multi-carbon products. However, challenges remain, including limited selectivity for certain products and insufficient electrochemical durability. To address these issues, substantial efforts have been dedicated to improving Cu-based catalysts[53-55]. In the following part, we explore various design strategies to enhance the efficiency of Cu-based catalysts for the selective conversion of CO_2 into C_{2+} [Table 2].

Defect engineering
Defects are crucial surface features that significantly influence a catalyst's performance by modifying its electronic properties and disturbing the periodic structure of the crystal, resulting in unique chemical and electronic characteristics[56,57]. Here, we highlight recently recent electrocatalysts that utilize defect engineering to enhance performance toward C_{2+} products and examine the influence of these defects in CO_2RR.

Vacancy
Enhancing the performance of Cu-based electrocatalysts has largely centered on investigating the role of vacancies, the most prevalent type of defect. These studies aim to explore how vacancies can be leveraged to optimize catalytic activity toward C_{2+} products. Xue *et al.* designed Cu/CeO_{2-x} catalysts featuring different levels of oxygen vacancies, investigating the interaction between Ce^{3+} and Cu species and its impact on catalytic performance[58]. The introduction of Cu into CeO_{2-x} generated a significant number of oxygen vacancies. Various Cu/CeO_{2-x} electrocatalysts were synthesized via the hydrothermal-reduction method

Table 2. Summary of catalysts for the reduction of CO_2 to C_{2+} products

	Catalyst	Main C_2 products (FE)	Current density	Reactor type	Ref.
Defect engineering	Cu/CeO_{2-x}-4	C_2H_4: 30% @-1.2 V_{RHE}	-	H-cell	[58]
	Cu/CeO_2	C_2H_4: 78.3% @ -1.0 V_{RHE}	-16.8 mA cm^{-2} @-1.0 V_{RHE}	H-cell	[59]
	1.0% I-CuO	C_2H_4: 50.2% @-1.2 V_{RHE}	J_{C2H4}: -9 mA cm^{-2} @-1.2 V_{RHE}	H-cell	[60]
	Sn-doped $CuO(V_O)$	C_2H_4: 48.5% ± 1.2% @-1.1 V_{RHE}	-	H-cell	[61]
	Cu SAs/UIO-H_2	C_2H_5OH: 46.28% @-0.66 V_{RHE}	-	Flow cell	[62]
	GB-Cu	C_2H_4: 38% @-1.2 V_{RHE}	J_{C2H4}: -37 mA cm^{-2} @-1.2 V_{RHE}	Flow cell	[65]
	GB-$Cu_{29.6}$	C_{2+} products: 73.2% @-3.8 V_{RHE}	-303.61 mA cm^{-2} @-3.8 V_{RHE}	MEA cell	[66]
	GB-Cu-IV	C_{2+} products: 68.2% @-1.28 V_{RHE}	J_{C2+}: -0.768 A cm^{-2} @-1.28 V	Flow cell	[67]
	RGBs-Cu	C_{2+} products: 77.3% @400 mA cm^{-2}	J_{C2+}: -353.6 ± 7.5 mA cm^{-2} @400mA cm^{-2}	Flow cell	[68]
Nanostructure engineering	3DOP Cu_2O–CO	C_{2+} products: 77.0% ± 0.3% @-0.88 V_{RHE}	J_{C2+}: -513.7±0.7 mA cm^{-2} @-0.88 V_{RHE}	Flow cell	[76]
	OD-Cu NWs	C_{2+} products: 77.7% @-0.51 V_{RHE}	J_{C2+}: -233.2 mA cm^{-2} @-0.51 V_{RHE}	Flow cell	[77]
	C-CuO nanosheets	C_2H_4: 56.2% @-0.871 V_{RHE}	J_{C2H4}: -171 mA cm^{-2} @-0.871 V_{RHE}	Flow cell	[78]
	Cu_2O-NS	C_{2+} products: 81.32% @-1.2 V_{RHE}	-187.6 mA cm^{-2} @-1.2 V_{RHE}	Flow cell	[79]
	f-Cu_2O	C_2H_5OH: 52.6% @-0.8 V_{RHE}	j_{C2H5OH}: -9.1 mA cm^{-2} @-0.9 V_{RHE}	H-cell	[80]
	Cu_{cub}	C_2H_4: 57% @-0.75 V_{RHE}	-	Flow cell	[81]
	NS-D Cu	C_{2+} products: 67.5% @-1.5 V_{RHE}	J_{C2+}: -25.1 mA cm^{-2} @-1.5 V_{RHE}	H-cell	[82]
	c-Cu_2O	C_2H_4: 61.3% @-1.2 V_{RHE}	J_{C2H4}: -2.5 mA cm^{-2} @-1.2 V_{RHE}	H-cell	[83]
	F-Cu_2O@ZIF-8	C_2H_4: 74.1% @-1.2 V_{RHE}	-	H-cell	[84]
	Copper NPs (25 nm)	C_{2+} products: 92.8% @-1.7 V_{RHE}	-	MEA cell	[85]
	$Cu_{45.2}$/GDY	C_{2+} products: 91.2% @-1.0 V_{RHE}	J_{C2+}: -312 mA cm^{-2} @-1.0 V_{RHE}	Flow cell	[86]
	HKUST-1-derived Cu clusters	C_2H_4: 45% @-1.07 V_{RHE}	-262 mA cm^{-2}@-1.07 V_{RHE}	Flow cell	[87]
	Cu_2-CuN_3	C_2H_5OH: 51% @-1.1 V_{RHE}	j_{C2H5OH}: -14.4 mA cm^{-2} @-1.1 V_{RHE}	H-cell	[88]
Surface modification	Cu foil+Gly	C_2H_4: 24% @-1.9 V_{RHE}	-	H-cell	[92]
	Cu/PANI	C_2H_4: 43.8% @-1.08 V_{RHE}	-28.3 mA cm^{-2} @-1.08 V_{RHE}	H-cell	[93]
	PANI/CuO NSs-25	C_{2+} products: 50% @-1.6 V_{RHE}	J_{C2H4}: -200.1 mA cm^{-2} @-1.6 V_{RHE}	H-cell	[94]
	Hydrophobic Cu dendrite	C_2H_4: 56% @-30 mA cm^{-2}	-	Flow cell	[95]
	TP-Cu	C_2H_4: 18.35% @-1.1 V_{RHE}	-	H-cell	[96]
	Cu-D	C_{2+} products: 64% ± 1.4% @-0.68 V_{RHE}	J_{C2+}: -255 mA cm^{-2} @-0.68 V_{RHE}	Flow cell	[97]
	S-Cu	C_{2+} products: 78% @-0.9 V_{RHE}	J_{C2+}: -1.81 Acm^{-2} @-0.9 V_{RHE}	Flow cell	[98]

Tandem strategy	Cu@Ag/C	C_2H_4: 58.03% @-0.85 V_{RHE}	J_{C2H4}: -49.41 mA cm^{-2} @-0.85 V_{RHE}	Flow cell	[105]
	Cu90Ag10	C_2H_4: 33.6% @2.2 V_{RHE}	J_{C2H4}: -42.70 mA cm^{-2}	MEA cell	[106]
	CuAg$_4$/EDTA	C_{2+}products: 86.56% @-1.23 V_{RHE}	J_{C2+}: -10 mA cm^{-2} @-1.23 V_{RHE}	H-cell	[107]
	Cu/Ag	C_2H_5OH: 57.5% @-1.1 V_{RHE}	j_{C2H5OH}: -356.7 ± 9.5 mA cm^{-2} @-1.1 V_{RHE}	Flow cell	[108]
	Ag$_1$–Cu$_{1.1}$NDs	C_2H_4: 38% @-1.1V_{RHE}	-1 mA cm^{-2} @-1.1 V_{RHE}	H-cell	[109]
	Ag$_{65}$–Cu$_{35}$ JNS-100	C_2H_4: 54% @-1.2 V_{RHE}	J_{C2H4}: -2 mA cm^{-2} @-1.2 V_{RHE}	H-cell	[110]
	Cu needle-Ag	C_{2+}products: 70% @300 mA cm^{-2}	J_{C2+}: -245 mA cm^{-2} @300 mA cm^{-2}	Flow cell	[111]
	Au/Cu	-	-15.29 mA cm^{-2} @-1.08 V_{RHE}	Flow cell	[112]
	S-2.0-Au@OD-Cu	C_2H_4: 40% @-300 mA cm^{-2}	J_{C2H4}: -115 mA cm^{-2} @-0.920 V_{RHE}	Flow cell	[113]
	Au$_{0.02}$Cu$_2$O	C_2H_4: 24.4 % @-1.3 V_{RHE}	-5.7 mA cm^{-2} @-1.3 V_{RHE}	H-cell	[114]
	Au@Cu-AuCu	0.9 µmol cm^{-2} h^{-1} @-1.0 V_{RHE}	-	H-cell	[115]
	Cu$_{99.3}$Au$_{0.7}$ NWs	C_{2+}products: 65.3% @-1.25 V_{RHE}	J_{C2+}: -12.1 mA cm^{-2} @-1.25 V_{RHE}	H-cell	[116]
	Au-Cu Janus NSs	C_{2+}products: 67% @-0.75 V_{RHE}	J_{C2+}: -0.29 A cm^{-2} @-0.75 V_{RHE}	Flow cell	[117]
	Cu$_2$O NCs-C-Copc	C_2H_4: 70.31 % @-0.76 V_{RHE}	J_{C2H4}: -226.18 mA cm^{-2} @-0.76 V_{RHE}	Flow cell	[121]
	Cu–CoPc	C_{2+}products: 82% @480 mA cm^{-2}	J_{C2+}: -394 mA cm^{-2} @480 mA cm^{-2}	Flow cell	[122]
	Cu$_2$O@CM	C_{2+}products: 73.2% @-1.1 V_{RHE}	J_{C2+}: -52.9 mA cm^{-2} @-1.1 V_{RHE}	H-cell	[123]
	Cu NPs/Ni–N–C	C_2H_4: 14.27 % @-0.9 V_{RHE}	J_{C2H4}: -1.67 mA cm^{-2} @-0.9 V_{RHE}	H-cell	[125]
	CuO/Ni	C_{2+}products: 81.4% @-1.1 V_{RHE}	J_{C2+}: -1220.8 mA cm^{-2} @-1.1 V_{RHE}	Flow cell	[126]
	Ni Pc + Cu-R	C_2H_4: 62 % @-500 mA cm^{-2}	J_{C2H4}: -370 mA cm^{-2} @-500 mA cm^{-2}	Flow cell	[127]
	PTF(Ni)/Cu	C_2H_4: 57.3% @-1.1 V_{RHE}	J_{C2+}: -3.1 mA cm^{-2} @-1.1 V_{RHE}	H-cell	[128]
	a-Ni/Cu-NP@CMK	C_2H_4: 72.3% @-1.1 V_{RHE}	J_{C2H4}: -294 mA cm^{-2} @-1.1 V_{RHE}	Flow cell	[129]
Non-cu based	Ni$_3$Al film	1-propanol: 1.9% @-1.38 V_{RHE}	-	H-cell	[130]
	Ni$_5$Ga$_3$	C_2H_6: 1.3% @-0.88 V_{RHE}	-	H-cell	[131]
	SnS$_2$/Sn$_1$-O$_3$G	C_2H_5OH: 82.5% @-0.9 V_{RHE}	j_{C2H5OH}: -14 mA cm^{-2} @-0.9 V_{RHE}	H-cell	[132]

RHE: Reversible hydrogen electrode; FE: faradaic efficiency; MEA: membrane electrode assembly; GBs: grain boundaries; OD-Cu: oxide-derived Cu; NSs: nanosheets; PANI: polyaniline; EDTA: ethylenediaminetetraacetic acid; NDs: nanodimers; PTF: porphyritic triazine framework; CMK: carbons mesostructured from Korea; RGBs: grain boundaries.

[Figure 3A]. High-resolution transmission electron microscopy (HRTEM) analysis demonstrated the presence of structural defects in the Cu/CeO$_{2-x}$-4 catalyst, as depicted in Figure 3B. The pristine CeO$_2$ catalyst in Figure 3C only produces H$_2$ and CO, regardless of the applied potential. However, the Cu/CeO$_{2-x}$-4 catalyst, which has the highest oxygen vacancy concentration, showed improved selectivity for C$_2$H$_4$ and CH$_4$ [Figure 3D and E]. Fang *et al.* investigated the integration of Cu into CeO$_2$ (Cu/CeO$_2$) using an impregnation-calcination method for CO$_2$RR[59]. The amount of Cu loading was controlled by adjusting
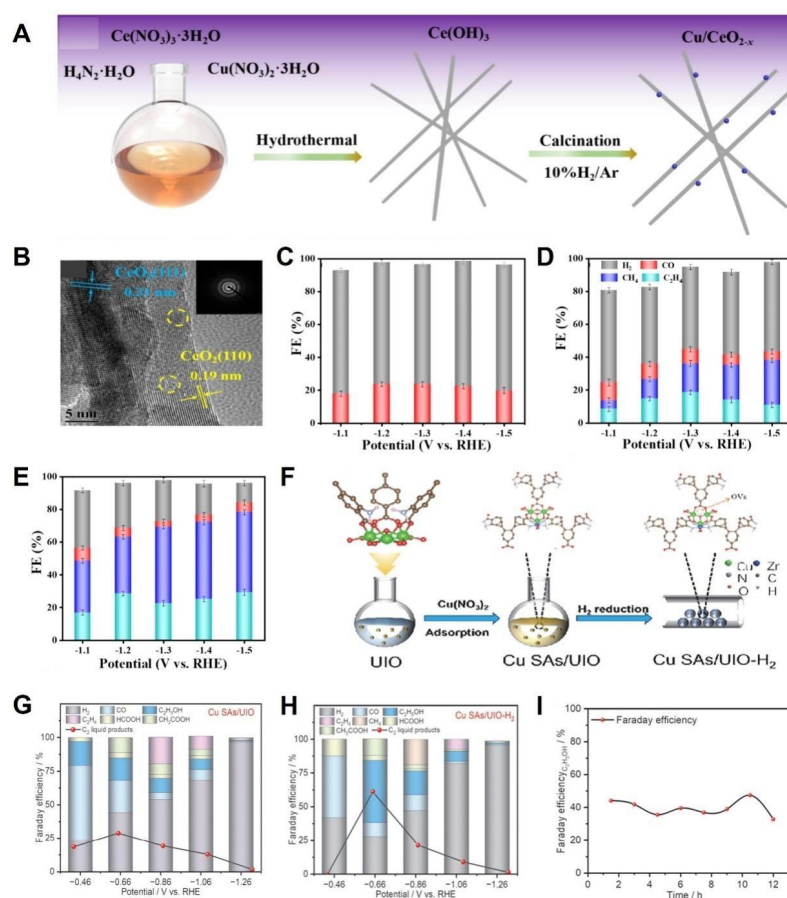
Figure 3. (A) Graphic representation of the Cu/CeO_{2-x}-4 catalyst synthesis; (B) HRTEM images of the Cu/CeO_{2-x}-4 catalyst; (C) FEs of bare CeO_2; (D) Cu/CeO_{2-x}-1; and (E) Cu/CeO_{2-x}-4. This figure is quoted with permission from Xue *et al.* Copyright (2024) Elsevier[58]; (F) Schematic representation of the synthetic process for Cu SAs/UIO-H_2; (G) The corresponding FEs for the reduction products of Cu SAs/UIO and (H) Cu SAs/UIO-H_2; (I) Long-term electrolysis of Cu SAs/UIO-H_2 at -0.66 V *vs.* RHE. This figure is quoted with permission from Bie *et al.* Copyright (2024) Elsevier[62].FE: Faradaic efficiency; HRTEM: high-resolution transmission electron microscopy; SAs: single atoms; RHE: reversible hydrogen electrode.

the concentration of the copper precursor during the impregnation process. The electrocatalytic performance for CO_2RR was analyzed in an H-cell with 0.1 M CsI as the electrolyte solution. Due to the strong electronic interaction of the Ce^{4+}-O^{2-}-Cu^+ structure of Cu/CeO_2 and the appearance of oxygen vacancies, the optimized catalyst featuring a Cu doping of 9.77 wt% achieved a C_{2+} Faradaic efficiency (FE) of 78.3% and a current density of 16.8 mA cm^{-2} at -1.0V *vs.* reversible hydrogen electrode (RHE). Recently, Shen *et al.* enhanced the performance of Cu catalysts for C_2H_4 production by introducing oxygen vacancies through iodine doping in CuO (I-CuO)[60]. Advanced characterization demonstrated that iodine doping facilitated the formation of Cu^+ species in CuO and increased the density of oxygen vacancies. Additionally, the introduction of iodine significantly enhanced the hydrophobicity of the catalyst, as evidenced by a contact angle of 131.1°, compared to the 0° of bare CuO. Electrocatalytic CO_2 reduction was assessed in an H-type cell, and liquid products were analyzed using hydrogen nuclear magnetic resonance spectroscopy (^1H NMR). Among the catalysts, 1.0% I-CuO presented the highest FE for C_2H_4 and the lowest for H_2 across the broad potential range of -1.0 V to -1.4 V *vs.* RHE. Notably, the FE_{C2H4} production reached up to 50.2%, which is 3.43 times greater than that of bare CuO. Additionally, the catalyst demonstrated stable performance over 15 h without any decline. Jiang *et al.* promoted ethylene production by optimizing the Sn doping and oxygen vacancies in CuO. The synergistic interaction between the Sn dopant and the oxygen

vacancies significantly facilitated the CO_2 electroreduction to C_2H_4[61]. Specifically, Sn-doped CuO (oxygen vacancies) achieved the highest FE_{C2H4} of 48.5% ± 1.2%, accompanied by a j_{C2H4} of 10.9 mA cm^{-2}, and demonstrated long-term durability over a period of 24 hours. Bie *et al.* structured atomically dispersed Cu atoms anchored on hydrogen-reduced UiO66-NH$_2$, characterized by abundant oxygen vacancies[62]. This catalyst, referred to as Cu single atoms (SAs)/UIO-H$_2$, was constructed through a hydrothermal process followed by a H$_2$-spillover treatment [Figure 3F]. As illustrated in Figure 3G and H, the FE for C$_{2+}$ products on Cu SAs/UIO reached a maximum of 27.71% at -1.06 V *vs.* RHE, which is significantly reduced compared to Cu SAs/UIO-H$_2$, highlighting the crucial role of oxygen vacancies in accelerating C-C coupling process. Furthermore, the Cu SAs/UIO-H$_2$ catalyst demonstrated a maximum FE of 46.28% for C_2H_5OH and 12.34% for acetic acid, with an overall FE for C$_{2+}$ products reaching 58.62%. The catalyst also exhibited excellent stability over 12 hours, maintaining an ethanol FE of approximately 46% at -0.66 V *vs.* RHE [Figure 3I].

Grain boundary

It is well established that grain boundaries (GBs) influence the selectivity of CO_2RR products[63], and a quantitative correlation has been observed between the density of GBs in Cu-based electrocatalysts and CO_2-to-C$_{2+}$ reduction[64]. As a result, GBs are regarded as a crucial factor in enhanced selectivity for C$_{2+}$ products of Cu-based catalysts. Enhancing GB density in Cu catalysts has been shown to significantly enhance C$_{2+}$ production. Chen *et al.* demonstrated the Cu electrodeposition with polyvinylpyrrolidone (PVP) as an additive allows for controlled grain growth[65]. The inert PVP adsorbed onto the Cu surface, accelerating the nucleation rate and reducing the size of crystal, resulting in a Cu electrode rich in GBs. The Cu electrode deposited without PVP is referred to as ED-Cu. When the GB-rich Cu electrode (GB-Cu) was used for eCO$_2$RR, it produced C_2H_4 and C_2H_6O across a broad potential range of -1.0 V to -1.3 V *vs.* RHE, achieving a high FE_{C2+} of 73%. Notably, GB-Cu showed C_2H_4 selectivity of ~38% at -1.2 V *vs.* RHE and a C_2H_6O-to-C_2H_4 ratio of 0.85 [Figure 4A and B]. *In situ* infrared absorption spectroscopy revealed that the GBs in Cu were key in facilitating the adsorption of $^{\cdot}CO$ intermediates, thereby promoting CO_2RR [Figure 4C]. Dendritic Cu catalysts with tunable GB were prepared by Zhang *et al.* using a pulsed electrochemical deposition method on the gas diffusion electrode (GDE)[66]. The GB density was adjusted by varying the deposition times to 50 ms, 100 ms, 200 ms, and 500 ms, with a constant pulse duration of 250 ms, all under a constant current density of 100 mA cm^{-2} [Figure 4D]. The high-angle annular dark-field scanning transmission electron microscopy (HAADF-STEM) image shown in Figure 4E revealed distinct high-contrast lines aligned parallel to the growth direction of the Cu dendrites, indicating a symmetrical lattice structure on either side, a typical feature of GBs. Notably, the selectivity for C$_{2+}$ products increased linearly with the GB density across all applied potentials. The GB-Cu$_{29.6}$ catalyst exhibited the highest FE_{C2+}, reaching 46.2%, along with a j_{C2+} of ~20 mA cm^{-2} at a potential of -1.1 V *vs.* RHE [Figure 4F and G]. Figure 4H shows activity mapping at a defined potential based on cyclic voltammetry, where GB-Cu$_{29.6}$ demonstrated distinct patterns of locally enhanced activity compared to Cu catalysts without GBs. This suggests that GBs facilitate electron transfer, thereby improving performance toward C$_{2+}$ productions.

Ding *et al.* introduced an innovative and straightforward salt-assisted annealing technique that induced unconventional grain fragmentation, significantly increasing the density of GBs[67]. The optimized electrocatalysts attained a maximum FE_{C2+} of 70.0% for the H-type cell and 68.2% for the flow cell, achieving a j_{C2+} of 0.768 mA cm^{-2} at -1.28 V *vs.* RHE, surpassing the performance of most previously reported counterparts. To investigate the correlation between GBs and the selectivity of the catalysts for C$_{2+}$ products, *in situ* Raman spectroscopy and Density functional theory (DFT) calculations were conducted. The results indicated that a greater GB density generates additional active sites for CO_2RR, resulting in a higher concentration of $^{\cdot}CO$ intermediate. This, in turn, promotes C-C coupling and ultimately increases C$_{2+}$ production. Kong *et al.* prepared small Cu nanoparticles (NPs) with enhanced small GBs (RGBs-Cu) using
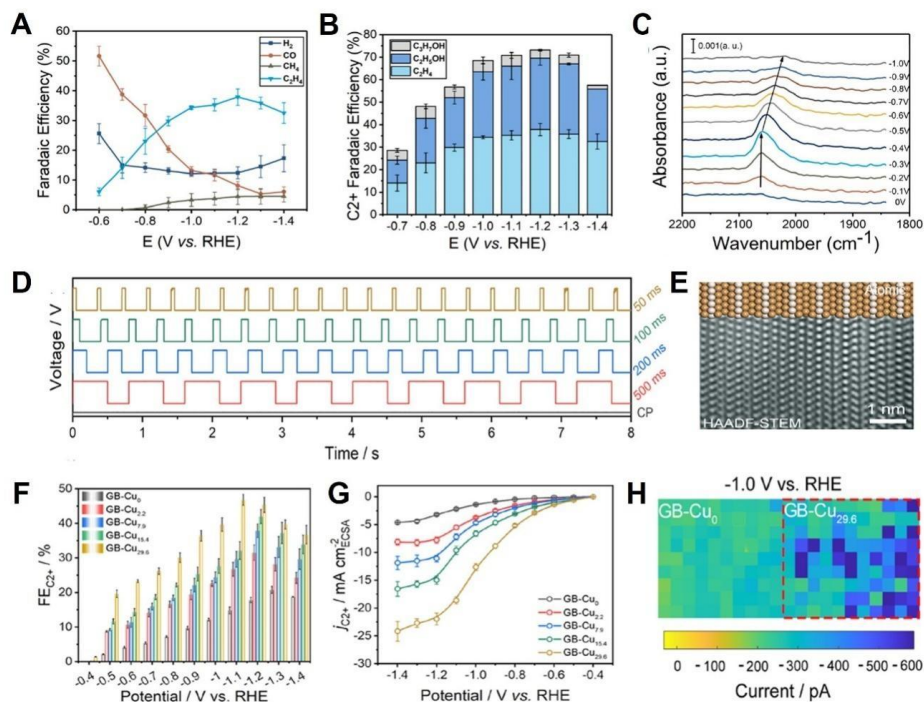
Figure 4. (A) FEs on GB-Cu; (B) $FE_{C_{2+}}$ of GB-Cu; (C) *In situ* ATR-SEIRAS spectra of GB-Cu. This figure is quoted with permission from Chen *et al.* Copyright (2020) American Chemical Society[65]; (D) Electrochemical deposition procedure for different Cu catalysts; (E) FFT-refined aberration-corrected HAADF-STEM image of the GB-Cu$_{29.6}$; (F) FEs for C_{2+} and (G) ECSA-normalized $j_{C_{2+}}$ of Cu with different GB densities; (H) Spatially resolved electrochemical map derived from the individual linear sweep voltammetry (LSV) curves. This figure is quoted with permission from Zhang *et al.* Copyright (2024) American Chemical Society[66]. FE: Faradaic efficiency; HAADF-STEM: high-angle annular dark-field scanning transmission electron microscopy; GBs: grain boundaries; ATR-SEIRAS: attenuated total reflectance-surface-enhanced infrared absorption spectroscopy; FFT: fast Fourier transform; ECSA: electrochemically active surface area.

spatial confinement and *in situ* electroreduction[68]. Figure 5A illustrates the schematic of the synthesis process for RGBs-Cu electrocatalysts, while HRTEM images reveal the numerous GBs present in the catalysts. CO_2RR electrolysis using the RGBs-Cu electrode was conducted using flow cells with different concentrations of KOH. Notably, elevating the KOH concentration to 2 and 3 M resulted in an additional enhancement of the FE for C_{2+} products, achieving 77.3% at a current density of 400 mA cm^{-2} in 2 M KOH [Figure 5B]. Additionally, RGBs-Cu reached a maximum C_{2+}-to-C_1 (C_{2+}/C_1) ratio of 2.57 at 400 mA cm^{-2}, which notably exceeded the control sample's ratio of 0.75 [Figure 5C]. Moreover, RGBs-Cu demonstrated exceptional stability, maintaining consistent C_{2+} selectivity of 60% over 134 h at a total current density of 500 mA cm^{-2} [Figure 5D].

Nanostructure engineering
Bulk Cu-based electrocatalysts suffer from limited exposed active sites and poor electronic structure, resulting in low CO_2RR performance towards C_{2+}[69,70]. To address these challenges, nanostructure engineering approaches-such as morphology control, facet optimization, and confinement effects-have appeared as powerful strategies to strengthen their catalytic efficiency for CO_2RR.

Confinement effect
Confinement structures in Cu-based electrocatalysts can enhance C_{2+} selectivity by increasing the retention time of intermediates such as $^*CO/^*COH$ by facilitating C-C coupling reactions[71,72]. Consequently, significant research has focused on tailoring the Cu surface with specialized confinement morphologies to
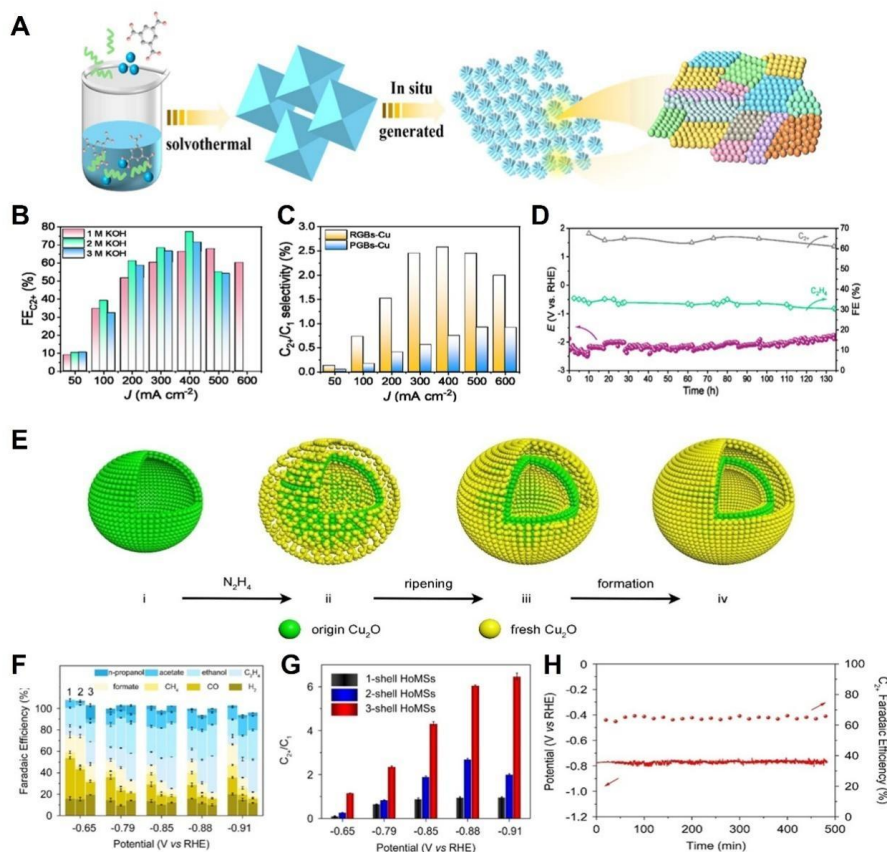
Figure 5. (A) Overview of the fabrication process of RGBs-Cu sample; (B) $FE_{C_{2+}}$ of RGBs-Cu with different electrolyte concentrations; (C) C_{2+}/C_1 product selectivity of RGBs-Cu and PGBs-Cu; (D) Evaluation of the long-term stability of the RGBs-Cu electrode at 500 mA cm^{-2} in a flow cell. This figure is quoted with permission from Kong *et al.* Copyright (2024) American Chemical Society[68]; (E) Schematic representation of Cu$_2$O HoMSs fabrication process; (F) Distribution of CO$_2$RR products on Cu$_2$O HoMSs catalysts 1-3 shell; (G) C_{2+}/C_1 product selectivity on HoMSs; (H) Long-term durability of 3-shell HoMSs for 8 h. This figure is quoted with permission from Liu *et al.* Copyright (2022) John Wiley and Sons[76]. FE: Faradaic efficiency; CO$_2$RR: CO$_2$ reduction reaction; HoMSs: hollow multi-shell structures; RGBs-Cu: Cu nanoparticle catalyst comprising abundant grain boundaries.

optimize both the activity and selectivity for C_{2+} product formation. Fan *et al.* fabricated three-dimensional (3D) ordered porous cuprous oxide cuboctahedra (3DOP Cu$_2$O-CO) through a hard templating method[73]. This method successfully created a structure characterized by ordered macropores that are interconnected with mesoporous channels throughout the Cu$_2$O cuboctahedra. The 3DOP-Cu$_2$O-CO configuration offers the benefits of uniformly distributed and interconnected pore channels. Consequently, these electrocatalysts demonstrated superior performance in CO$_2$RR compared to control catalysts lacking ordered porous architectures. Notably, 3DOP-Cu$_2$O-CO achieved a significant electrochemical double-layer capacitance of 2.9 mF cm^{-2}, with a maximum C_{2+} FE of 73.4% at -1.4 V *vs.* RHE in an H-cell, and 81.7% at -1.0 A cm^{-2} using a flow-type cell. Finite element method (FEM) simulations demonstrated that the structured pore architecture of 3DOP Cu$_2$O-CO capably confines and holds adequate *CO for adsorption during the CO$_2$ reduction process, thereby facilitating the strong dimerization required for C_{2+} product formation. Liu *et al.* designed distinctive Cu-based catalysts with a cavity structure, achieved through *in situ* electrochemical reduction of Cu$_2$O cavities[74]. Both transmission electron microscopy (TEM) and scanning electron microscopy (SEM) analyses confirmed the presence of cavity architecture. FEM simulations also confirmed that the cavity structure significantly enhances the concentration of CO intermediates at the reaction site, thereby promoting the C-C coupling reaction. These Cu cavity catalysts demonstrated excellent C_{2+} FE of

75.6 ± 1.8% and achieved $j_{C_{2+}}$ of 605 ± 14 mA cm^{-2} in a microfluidic flow cell. Moreover, the experimental C_{2+}/C_1 of Cu cavity catalysts reached the maximum of 5.4 ± 0.6. Pan *et al.* investigated the use of hollow mesoporous carbon spheres (HMCS) to explore the influence of confinement on the production of C_{2+} products[75]. They prepared a series of Cu-incorporated HMCS with copper loadings of 10%, 20%, and 30%, designated as Cu/HMCS5-10%, Cu/HMCS5-20%, and Cu/HMCS5-30%, respectively. The results revealed that Cu/HMCS$_5$-20% achieved the greatest FE$_{C_{2+}}$ of 88.7%, outperforming 69.3% and 80.1% FE$_{C_{2+}}$ recorded for Cu/HMCS$_5$-10% and Cu/HMCS$_5$-30%, respectively, at a potential of -1.0 V *vs.* RHE in a 1.0 M KOH solution. Notably, Cu/HMCS$_5$-20% exhibited remarkable stability, maintaining its performance over 20 h at -1.0 V *vs.* RHE without significant degradation. The exceptional C_{2+} selectivity of Cu/HMCS$_5$-20% was attributed to the unique confinement effects provided by HMCS, along with the synergistic interactions among Cu atoms with varying oxidation states. Liu *et al.* described the development of Cu_2O hollow multi-shell structures (HoMSs) with adjustable shell numbers[76]. The synthesis of Cu_2O HoMSs was accomplished using the Ostwald ripening method, as depicted in Figure 5E. Electrocatalytic CO_2 reduction was conducted in a flow reactor using 0.5 M KHCO$_3$. Prior to testing, Cu_2O HoMSs underwent electroreduction at -0.82 V *vs.* RHE for ten minutes. Notably, the Cu_2O structure with three shells reached a peak C_{2+} FE of 77.0 ± 0.3%, outperforming the 1-shell (40.3 ± 1.0%) and 2-shell (62.2 ± 0.3%) counterparts at -0.88 V *vs.* RHE [Figure 5F]. The increase in shell number clearly enhanced C_{2+} production [Figure 5G]. Furthermore, the 3-shell HoMS catalysts exhibited excellent long-term stability, maintaining performance for 8 h at -300 mA cm^{-2}, underscoring the advantages of the nanoconfinement effect in converting CO_2 to C_{2+} products [Figure 5H].

Morphology/facet effect
Aside from confinement engineering, the morphology and crystal facets of Cu-based electrocatalysts have a fundamental role in influencing CO_2 electroreduction activity and product selectivity. For example, Wu *et al.* revealed a correlation between the structural dimensions of oxide-derived Cu (OD-Cu) electrocatalysts and their ability to selectively produce C_{2+} products[77]. Their study involved the synthesis of three distinct nanostructures: one-dimensional nanowires (NWs), two-dimensional nanosheets (NSs), and 3D nanoflowers (NFs), all of which displayed notable resistance to structural degradation [Figure 6A]. Initial evaluations of the CO_2RR activity and the electrochemical characteristics of the OD-Cu catalysts were conducted using H-cell systems. As demonstrated in Figure 6B, the product distribution from CO_2RR over the OD-Cu catalysts was evaluated across a potential range from -0.6 V to -1.4 V *vs.* RHE. Of the three morphologies, OD-Cu NWs achieved the highest preference for C_{2+} products, reaching a maximum FE of 50.2% at -1.4 V *vs.* RHE, which notably surpassed the performance of OD-Cu NSs (35.6%) and NFs (13.3%). Additionally, the performance of OD-Cu catalysts was additionally evaluated with flow cells. Notably, OD-Cu NWs, which have the maximum surface Cu-O coordination, exhibited the most favorable CO_2RR kinetics for C_{2+} production, achieving 77.7% of FE$_{C_{2+}}$, 233.2 mA cm^{-2} for $j_{C_{2+}}$, 701.8 µmol h^{-1} cm^{-2} of C_{2+} yield, and 51.1% C_{2+} energy efficiency [Figure 6C]. Additionally, OD-Cu NWs exhibited remarkable stability, maintaining consistent CO_2RR performance at 300 mA cm^{-2} for 72 h.

Moreover, Cu-based catalysts with a two-dimensional NS morphology are appealing due to their plentiful low-coordination edge sites, which are frequently regarded as essential for improving catalytic performance. Xie *et al.* synthesized Cu NSs derived from CuO during CO_2RR, having an average size of approximately 30 nm and thickness of about 20 nm[78]. With an abundant concentration of low-coordination edge sites, these Cu NSs enabled efficient C-C coupling reactions, reaching a peak FE$_{C2H4}$ of 56.2% and a j_{C2H4} of 171.0 mA cm^{-2} at -0.871 V *vs.* RHE in a flow cell. Wang *et al.* developed thin-layered Cu_2O NSs having thickness of 0.9 nm (Cu_2O-NS) via coprecipitation method[79]. For comparison, other ultrathin catalysts, Cu-NS and CuO-NS, were also fabricated. The Cu_2O-NS demonstrated a total current density of
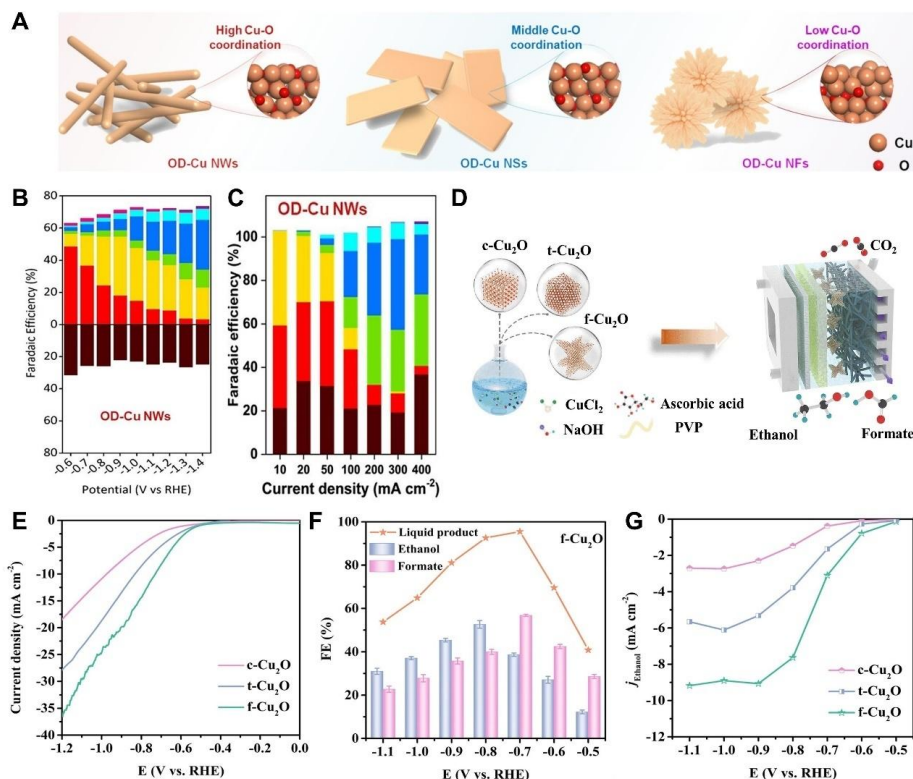
Figure 6. (A) Diagram illustrating the preparation of OD-Cu catalysts with different morphologies; (B) $FE_{C_{2+}}$ of OD-Cu NWs using H-cell; (C) $FE_{C_{2+}}$ of OD-Cu NWs using flow cells. This figure is quoted with permission from Wu *et al.* Copyright (2024) Elsevier[77]; (D) Schematic illustration for the synthesis of various Cu_2O; (E) LSV curves of all three catalysts; (F) FEs of various liquid products on f-Cu_2O; (G) j_{C2H6O} on f-Cu_2O. This figure is quoted with permission from Yang *et al.* Copyright (2024) Elsevier[80]. OD-Cu: Oxide-derived Cu; NWs: nanowires; LSV: linear sweep voltammetry; FE: faradaic efficiency.

-187.6 mA cm^{-2} and a FE of 81% for C_{2+} products, with $FE_{C_2H_4}$ reaching 40%, and stability of ten hours. The remarkable CO_2RR performance is attributed to coordination defects and oxygen vacancies, which enhanced ${}^*CO$ adsorption and improved C_{2+} product selectivity by stabilizing the surface oxidation state of Cu.

Facet engineering is essential in defining the catalyst's activity toward desired products. This can be achieved through various methods. Yang *et al.* explored the impact of morphology on the performance of Cu_2O catalysts for the production of liquid products[80]. Cu_2O electrocatalysts with various morphologies were synthesized using PVP as a capping agent. A schematic representation of the synthesized catalysts, including cube-shaped Cu_2O (c-Cu_2O), tetrakaidecahedron-shaped Cu_2O (t-Cu_2O), and flower-like Cu_2O (f-Cu_2O), is provided in Figure 6D. Surface coordination-unsaturated Cu atoms on the (111) facet were observed to improve CO_2 reduction by facilitating the adsorption of CO_2 molecules. Oxygen vacancies were confirmed using electron paramagnetic resonance spectroscopy and ultraviolet-visible diffuse reflection spectroscopy. Figure 6E presents the linear sweep voltammetry (LSV) curves of the Cu_2O catalysts in an H-cell, showing that the f-Cu_2O with exposed (111) facets exhibited higher current density and a minimized onset potential. The selectivity toward liquid products was further assessed using ${}^1H$ NMR. At -0.8 V *vs.* RHE, the f-Cu_2O catalyst achieved an ultimate C_2H_6O FE of 52.6% and a j_{C2H6O} of 9.1 mA cm^{-2} at -0.9 V *vs.* RHE, attributed to the abundance of oxygen vacancies on its surface [Figure 6F and G]. Furthermore, the ethanol formation rate on f-Cu_2O rose markedly from 0.43 µmol h^{-1} cm^{-2} at -0.5 V to 28.56 µmol h^{-1}cm^{-2} at -1.1 V *vs.* RHE. Significantly, the ethanol production rate on the f-Cu_2O catalyst was 3.4 times higher than

that of c-Cu_2O and 1.6 times greater than that of t-Cu_2O. Gregorio *et al.* demonstrated facet-dependent selectivity on the Cu electrode, achieved through morphology adjustment via colloidal chemistry[81]. Aligned with prior findings, Cu nanocubes enclosed by (100) facets show superior selectivity for C_2H_4, while Cu electrocatalysts with (111) facets demonstrate the highest selectivity toward CH_4. Fu *et al.* revealed that Cu catalysts with exposed (100) facets exhibit significantly higher selectivity for C_{2+} products compared to those with (111) and (110) facets[82]. They developed three types of catalysts with distinct morphologies-NWs, NPs, and NSs-each exposing different crystal facets through pre-reduction and reconstruction methods. Among them, the NS-D Cu catalyst, characterized by its (100) facet, was particularly effective at enhancing *CO adsorption, increasing surface *CO coverage, and facilitating CO dimerization, thereby boosting its activity for C_{2+} product formation. This catalyst achieved a FE of 67.5% towards C_{2+} products, a $j_{C_{2+}}$ of 25.1 mA cm^{-2}, and maintained stable performance for ten hours. Additionally, the NS-D Cu showed a maximum C_{2+}/C_1 ratio of 6.2, surpassing NW-D Cu and NP-D Cu, with ratios of 1.7 and 1.9, respectively.

Dong *et al.* proposed a novel mechanism elucidating the link between the crystal facets of Cu_2O and the formation of distinct reduction products[83]. Through a combination of theoretical calculations and experimental validation, they supported their findings. The exposed Cu atoms on the (100) facet displayed a dense Cu_4O_1 surface coordination, which enhanced the adsorption of *CO intermediates. Consequently, Cu_2O with the (100) facet showed significantly higher selectivity for C_2H_4 in 0.1 M $KHCO_3$ solution, achieving a FE for C_2H_4 of 61.3% at 1.2 V *vs.* RHE. Compared to other Cu-based catalysts reported in recent studies, their Cu_2O with (100) facets demonstrated superior selectivity toward C_2H_4. Luo *et al.* synthesized six distinct morphologies of Cu_2O NPs using $NH_2OH \cdot HCl$ as a reductant, each exposing different crystal facets, and then applied a ZIF-8 shell to improve their stability [Figure 7A][84]. The NPs, labeled A-Cu_2O through F-Cu_2O, were obtained by varying the amount of $NH_2OH \cdot HCl$. Figure 7B and C illustrates the electrochemical performance of these Cu_2O catalysts in 0.1 M $KHCO_3$ over a potential range of -0.7 V to -1.3 V *vs.* RHE. Among them, F-Cu_2O, which primarily exposed the (332) facet, showed the highest FE_{C2H4} production, reaching 74.1% at -1.2 V *vs.* RHE. It was also observed that increasing the proportion of (111) facets significantly enhanced both the selectivity and activity of as synthesized electrocatalysts. DFT calculations further confirmed that the (332) facet, with its step-like structure, substantially lowered the Gibbs free energy for *CHO intermediate coupling, leading to improved electrocatalytic performance.

Size effect
Another approach to develop electrocatalysts is controlling the size of electrocatalysts. Reducing the size increases the surface-to-volume ratio, thereby enhancing the utilization of metal atoms. Additionally, the number of undercoordinated sites increases, leading to a perturbed electronic structure and enhanced activity.

Merino-Garcia *et al.* investigated the selectivity and activity of the catalyst based on the size of the Cu particles, which were synthesized with sizes ranging from 25 nm to 80 nm[85]. Cu particles of different sizes were mixed with a binder and isopropanol to prepare a GDE by depositing the mixture onto carbon paper. The electrode with 25 nm Cu particles exhibited significantly better performance compared to those with Cu particle sizes of 40-60 nm and 60-80 nm, achieving a remarkably high ethylene FE of 92.8% and a production rate of 1,148 µmol m^{-2} s^{-1}. This enhanced performance is attributed to an increase in the fraction of under-coordinated sites as the particle size decreases. Furthermore, Rong *et al.* explored the size effects of Cu catalysts, ranging from SAs to nanoclusters, using a facile acetylenic-bond-directed site-trapping approach[86]. Three different catalysts of varying sizes were synthesized: single-atoms (~0.1 nm), subnanometric clusters (0.5~1 nm) and nanoclusters (1~1.5 nm). They demonstrated that increasing the size of Cu nanoclusters enhanced both catalytic activity and selectivity toward C_{2+} products. The
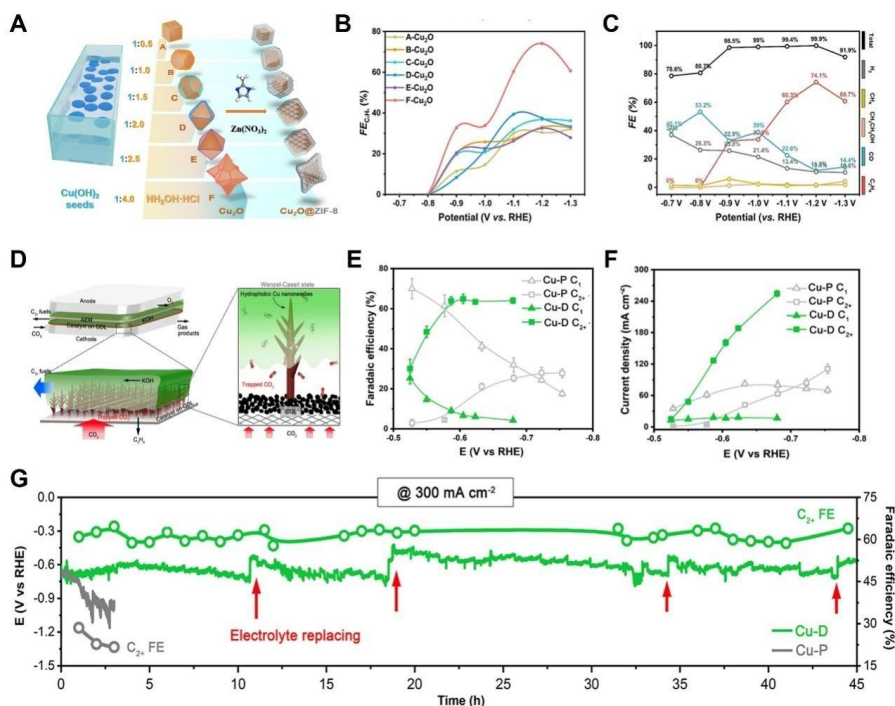
Figure 7. (A) Preparation of Cu_2O nanoparticles and Cu_2O@ZIF-8 composites; (B) FE_{C2H4} of Cu_2O nanoparticles with different facets; (C) FE of products on $F-Cu_2O$ at different potentials. This figure is quoted with permission from Luo *et al.* Copyright (2022) John Wiley and Sons[84]; (D) Schematic illustration for the synthesis of various Cu_2O; (E) C_{2+} and C_1 faradaic efficiencies; (F) j_{C2+} on Cu-D and Cu-P; (G) Durability analysis for the Cu-D and Cu-P electrodes at 300 mA cm^{-2}. This figure is quoted with permission from Niu *et al.* Copyright (2021) American Chemical Society[97]. FE: Faradaic efficiency.

electrocatalytic performance was assessed in a three-compartment flow cell. Among the synthesized catalysts, the optimized Cu-based nanoclusters with a size of 1-1.5 nm exhibited the best performance, achieving a FE_{C2+} of 91.2%, a partial current density of 312 mA cm^{-2}, and moderate stability lasting approximately 22 h. Nam *et al.* synthesized Cu clusters using copper benzene-1,3,5-tricarboxylate (HKUST-1) as a precursor[87]. The calcination time was controlled to remove benzene tricarboxylate moieties, resulting in Cu dimer distortion and the generation of undercoordinated Cu sites within the Cu clusters. HKUST-1 calcined at 250 °C for 3 h exhibited the lowest Cu-Cu Coordination number of 9.5 ± 0.9 among the synthesized Cu clusters. The electrocatalytic performance of the catalysts was evaluated in a flow cell with 1 M KOH. Among the samples, HKUST-1 calcined at 250 °C for three hours showed the highest selectivity for C_2H_4, achieving a FE_{C2H4} of 45%, significantly outperforming the as-prepared HKUST-1 (FE_{C2H4}=10%). Su *et al.* synthesized electrocatalysts consisting of CuO clusters anchored on N-doped carbon NSs ($Cu/N_{0.14}C$)[88]. Cu/N_xC with varying nitrogen contents was prepared in two steps: (1) simple mixing of copper phthalocyanine and dicyandiamide followed by drying, and (2) pyrolysis of the dried mixture at different temperatures. The optimized $Cu/N_{0.14}C$ catalyst exhibited a superior FE_{C2+} of 73%, with a selectivity towards ethanol of 51% and a partial current density of 14.4 mA cm^{-2} at -1.1 V *vs.* RHE. Moreover, it demonstrated excellent long-term durability, maintaining stable FE_{C2+} and partial current density for over ten hours.

Surface modification

While earlier studies primarily concentrated on aspects such as composition, morphology, size, crystal structure, and internal electronic properties, recent research has shifted toward optimizing the surface microenvironment. Surface modification has emerged as a powerful strategy to improve CO_2 reduction to

C_{2+} products through the adjustment of properties such as hydrophobicity, electronic structure, and the adsorption energy of CO_2RR intermediates on the catalyst surface[89-91]. Introducing molecules such as long-chain alkyls or polymers to Cu-based catalysts can suppress H_2 production and improve catalytic stability.

Xie *et al.* introduced a strategy for modifying Cu electrodes using amino acids. After modifying the surface of Cu NWs with a series of amino acids, the CO_2RR performance toward the generation of C_{2+} products significantly improved[92]. Theoretical calculations suggested that -COOH and -NH_2 groups in amino acids enhance the C_{2+} selectivity by stabilizing and transforming $^*CHO$ intermediates while inhibiting the HER. Wei *et al.* applied polyaniline (PANI) to modify the catalytic performance and selectivity of Cu[93]. By coating a PANI thin film, approximately 50 nm thick, on the Cu electrode, the chemical environment of the Cu surface was altered, resulting in an excellent C_{2+} FE of 60%, which is almost four times higher than that of the bare Cu electrode at -1.1 V *vs.* RHE. Similarly, Ma *et al.* explored the effect of polymer modification on the CO_2 electroreduction performance and C_{2+} selectivity using PANI[94]. PANI NPs were coated on the surfaces of CuO NSs by a wet-chemical polymerization method. The PANI/CuO NSs hybrids were optimized by controlling the loading amount of PANI. The electrocatalytic performance toward CO_2RR was evaluated using a three-electrode H-type cell. Compared to CuO NSs without the PANI, the optimized catalysts demonstrated excellent selectivity and durability, achieving a FE of up to 66.4% and long-term stability of 92 h at -1.6 V *vs.* RHE. Consequently, decorating CuO NSs with PANI NPs not only boosts their stability but also increases local $^*CO$ surface coverage, owing to the distinctive relationship between the -NH- group and adsorbates. This interaction further promoted superior C-C coupling at the neighboring Cu active sites, facilitating the formation of C_{2+} products. Wakerley *et al.* demonstrated a highly hydrophobic Cu dendrite electrode using the 'plastron effect,' similar to the mechanism used by aquatic arachnids, through 1-octadecanethiol treatment[95]. Owing to its superhydrophobic characteristics, the corresponding electrode exhibited low H_2 evolution even at -1.6 V *vs.* RHE. Conversely, the Cu electrode that underwent surface modification attained a FE of 56% for C_2H_4 and 17% for C_2H_6O production, in contrast to 9% and 4% for its hydrophilic, wettable counterpart. However, the superhydrophobicity nature of the electrode surface obstructs the active sites participating in the reaction, resulting in a reduction in current density. Moreover, the stability of superhydrophobicity during the electrochemical CO_2 reduction process has not been clearly elucidated. To address these issues, Shi *et al.* revealed the effect of interface evolution on CO_2RR performance using 1-octadecanethiol modification. The interface where catalysis occurs changed from hydrophilic to hydrophobic, ultimately forming a stable triple-phase interface (TP-Cu)[96]. We examined characteristics of the electrode during the evolution using SEM, contact angle measurements, X-ray photoelectron spectroscopy (XPS), finding that the Cu dendrite structure was well preserved and the 1-octadecanethiol surface layer remained on the surface without desorption. However, it was observed that wettability changed as the operating time increased. Furthermore, the alkane thiol-modified copper surface eventually transitioned to a robust copper thiolate form under reaction conditions. Remarkably, this evolution reduced charge transfer resistance and allowed for higher accessibility of active sites, facilitating optimized gas-liquid-solid interface. Consequently, TP-Cu demonstrated a significant reduction in H_2 production compared to the initial hydrophobic surface. Niu *et al.* designed a nature-inspired copper catalyst on a gas diffusion layer, modeled after plants with hydrophobic characteristics, such as Setaria[97]. A scalable electrodeposition method was used to fabricate a hierarchical Cu catalyst with fine needles on a gas diffusion layer (GDL) [Figure 7D]. Unlike other reported literature, these CO_2RR electrodes exhibited stable hydrophobicity without requiring a hydrophobic coating. The CO_2 electroreduction activity of the Cu electrodes was evaluated by a flow cell operating with 1 M KOH. As the negative potential increased from -0.53 V to -0.68 V *vs.* RHE, FE of C_1 products decreased, while the selectivity towards C_{2+} products increased, due to enhanced C-C coupling. Specifically, the electrode achieved a high C_{2+} production rate of 255 ± 5.7 mA cm^{-2} with a 64 ± 1.4% $FE_{C_{2+}}$, demonstrating exceptional

stable performance at 300 mA cm^{-2} for more than 45 h [Figure 7E-G]. Recently, Liu *et al.* innovated a facile surface modification using toluene molecules to mitigate the degradation of catalysis performance[98]. Additionally, stearic acids were functionalized on the surface of the Cu catalyst (S-Cu). Through π-π interactions, the hydrophobic and conjugated benzene rings of toluene organized into structured hydrophobic micro-channels with a spacing of about 5.1 Å. In contrast, the spacing between adjacent stearic acids was calculated to be 2.3 Å, smaller than the sizes of H_2O or CO_2 molecules, leading to lower selectivity for C_{2+} products. Furthermore, molecular dynamics (MD) simulations were performed to examine the microenvironment on the surface of the catalyst throughout CO_2RR. MD simulations indicated that the three samples exhibited different distributions of CO_2 and H_2O, resulting in different CO_2RR performances. Notably, T-Cu demonstrated the highest performance, surpassing both pristine and S-Cu, with a FE_{C2+} of 78%, a j_{C2+} of 1.81 A cm^{-2}, and excellent stability for 400 h.

Tandem strategy

Among the various strategies to boost the activity of electrochemical CO_2 reduction, the tandem strategy has been acknowledged as a promising strategy. Tandem catalysts are designed with dual active sites, allowing them to influence intermediates and achieve faster reaction rates compared to Cu monometallic components[99-101]. Important intermediates formed at one active site can be transported to another site to engage in subsequent electrochemical reduction. In particular, the *CO intermediate is essential for the generation of C_{2+} products[102]. Zn, Ag, and gold (Au) provide additional CO to amplify *CO surface coverage on Cu active sites, promoting C-C coupling and elevating C_{2+} product formation. However, if *CO undergoes further reduction without coupling to form *CHO or *COH, CH_3OH or CH_4 will be produced. Therefore, enhancing *CO intermediate coverage and facilitating coupling reactions is a key strategy to improve selectivity for C_{2+} products[103,104].

Ag-based

Ag is known for its high activity in CO production and is one of the most commonly used metals as a component in tandem catalysts. Although its CO selectivity is lower than that of Au, it is suitable for use in tandem catalysts from a cost perspective.

Recently, Duan *et al.* fabricated Cu@Ag/C via *in-situ* electrochemical reconstruction of $Cu_2CO_3(OH)_2$/AgCl/C composite[105]. $Cu_2CO_3OH)_2$/AgCl/C was first synthesized by precipitating different amounts of AgCl, followed by electroreduction using an H-type reactor. The performance of the Cu@Ag/C catalyst was assessed in an H-type cell with 0.1 M KCl. As depicted in Figure 8A, the FE_{C2H4} achieved 50.41% at -1.1 V *vs.* RHE, which is 1.7 times superior to bare Cu/C catalysts (30.41%). We further compared the FE_{CO} of Cu@Ag/C and Cu/C to emphasize the role of Ag in promoting CO production [Figure 8B]. The incorporation of Ag significantly enhanced CO formation, increased *CO coverage, and consequently promoted C-C coupling, contributing to the formation of C_2H_4. Moreover, electrocatalytic performance was evaluated using flow-type cells to improve CO_2 mass transfer. Cu@Ag/C demonstrated a maximum FE_{C2H4} of 58.03% at -0.85 V *vs.* RHE, as shown in Figure 8C. Jeon *et al.* prepared bimetallic catalysts with varied Cu/Ag ratios by ultrasonic spray pyrolysis process[106]. The electrochemical performance of Cu_XAg_{100-X} catalysts was evaluated in a single cell across a voltage range of 1.8 to 2.3 V. As expected, only CO and H_2 were produced with Ag_{100}, while C_2H_4, CH_4, CO, and H_2 were produced with the Cu-containing catalyst. Moreover, Cu-containing catalysts showed a decrease in FE_{CO} and an increase in FE_{C2H4} at potentials that favor C_2H_4 production. This is because a crucial step in C_2H_4 formation involves the C-C coupling reaction, which consumes CO as a reactant. The optimized Cu_XAg_{100-X} with a ratio of 9:1 demonstrated the highest FE_{C2H4} of 33% at a cell voltage of 2.2 V, which is significantly higher than that of bare Cu (22%). Recently, Liu *et al.* constructed Cu-Ag tandem catalysts utilizing ethylenediaminetetraacetic acid (EDTA) as a ligand, leveraging ligand modification in CO_2RR[107]. Here, EDTA played a dual role in modulating both the
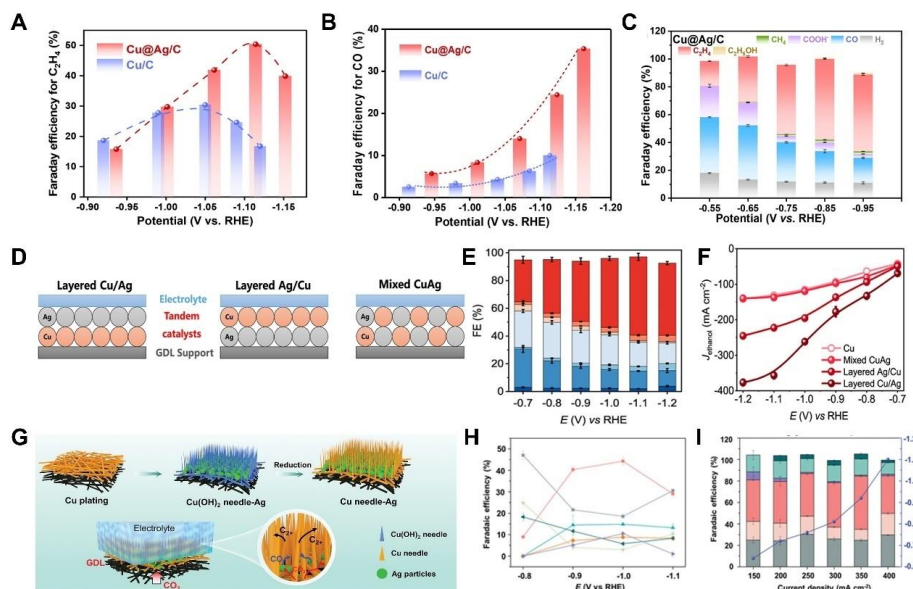
Figure 8. (A) FE distribution of C_2H_4 on Cu/C and Cu@Ag/C catalysts; (B) FE_{CO} on Cu/C and Cu@Ag/C catalysts; (C) FE of various products on Cu@Ag/C at various potentials. This figure is quoted with permission from Duan *et al.* Copyright (2024) Elsevier[105]; (D) Schematic illustration of three types of tandem catalysts; (E) FEs of products on layered Cu/Ag; (F) Partial current density of ethanol on Cu, mixed CuAg, layered Ag/Cu, and layered Cu/Ag catalysts. This figure is quoted with permission from Luan *et al.* Copyright (2024) American Chemical Society[108]; (G) Schematic diagrams of Cu needle-Ag tandem catalysts; (H) FEs for H_2, C_2H_4, CH_4, $HCOO^-$, C_2H_5OH, CO, and propanol on Cu needle-Ag catalysts; (I) FEs for different products of the Cu needle-Ag tested in a flow cell. This figure is quoted with permission from Wei *et al.* Copyright (2023) John Wiley and Sons[111]. FE: Faradaic efficiency.

electrode structure and the local pH around the surface Cu atoms during the electrochemical process. Cu-Ag tandem catalysts modified with EDTA (CuAg$_4$/EDTA) exhibited an excellent FE_{CO} at low potentials, and achieved an $FE_{C_{2+}}$ of 86.56%, compared to Cu (44.13%), CuAg$_4$ (33.32%) and Cu/EDTA (52.15%). Luan *et al.* developed a tandem catalyst designed for C_2H_6O production. Several electrode configurations were fabricated, including layered Cu/Ag, layered Ag/Cu, and mixed CuAg structures [Figure 8D][108]. The layered Cu/Ag catalyst exhibited outstanding electrochemical performance for CO_2-to-C_2H_6O conversion compared to other types of electrodes and bare Cu catalysts. Remarkably, the best-performed layered Cu/Ag electrode achieved a FE of 56.5 ± 2.6% for C_2H_6O and a current density of 356.7 ± 9.5 mA cm^{-2} at -1.1 V *vs.* RHE [Figure 8E and F]. This elevated performance, compared to the inverse layered Ag/Cu structure, can be credited to the efficient mass transport of CO gas produced in the Ag catalyst layer (CL). Huang *et al.* constructed Ag-Cu nanodimers (NDs) by establishing Cu domains onto pre-existing Ag NPs, resulting in an adjustable interface between the two distinct metals[109]. This arrangement strengthened CO adsorption on the surface, promoting the conversion of CO into C_2H_4, resulting from electron depletion in Cu due to electron migration from Cu to the Ag domains. Consequently, the Ag-Cu NDs with an Ag and Cu in a 1:1.1 mass ratio showed a notable increase in both the FE for C_2H_4 and the j_{C2H4} compared to bare Cu NPs. Similarly, Ma *et al.* described the preparation of Janus-like Ag-Cu nanostructures, where Cu having exposed (100) facets was restricted to one of the six equivalent faces of Ag nanocubes[110]. Compared to Cu nanocubes, the resulting Ag$_{65}$-Cu$_{35}$ Janus nanostructures with (100) facets (Ag$_{65}$-Cu$_{35}$ JNS-100) demonstrated a substantially advanced FE for C_4H_4 production, reaching 54%, with a total C_{2+} product efficiency of 72%. Additionally, the selectivity of the optimized Ag$_{65}$-Cu$_{35}$ JNS-100 toward C_2H_4 surpassed that for CH_3CH_2OH and CH_3COOH, with FEs of 1.7% and 4.2%, respectively. These enhanced results were due to CO induced on the Ag domains, which could migrate to the Cu (100) facets, promoting dimerization on the Cu surface owing to electron flow between Ag and Cu.

In a tandem catalyst system, two main pathways are involved: (1) CO_2 is first reduced to CO by a metal with high CO selectivity, and (2) the generated CO then migrates to neighboring Cu sites, where it undergoes C-C coupling and hydrogenation to form C_{2+} products. However, if the initial CO formation occurs too rapidly, C-C coupling may be limited, leading to higher selectivity for CO over C_{2+} products. Extending the residence time of CO on Cu active sites increases the likelihood of CO absorption and further reduction, thereby decreasing the FE_{CO} and enhancing the $FE_{C_{2+}}$. Thus, controlling CO residence time on Cu sites is a key factor in optimizing tandem catalyst systems. Wei *et al.* fabricated a 3D tandem catalyst by depositing Ag NPs at the base of Cu nanoneedle arrays to control the transport distance of CO [Figure 8G][111]. The electrocatalytic performance of the obtained tandem catalyst was initially measured in an H-type cell. Compared to a similar structure lacking Ag NPs at the base, the Cu needle-Ag achieved a selectivity of 45.6% for C_2H_4 at -1.0 V *vs.* RHE [Figure 8H]. Additionally, Cu needle-Ag catalysts were evaluated in a flow cell to achieve commercially relevant current densities. As depicted in Figure 8I, the Cu needle-Ag catalyst demonstrated exceptional selectivity towards C_{2+} products across applied current densities between 200 mA cm^{-2} to 350 mA cm^{-2}. Specifically, the FE for C_{2+} products rose from 58.2% at 100 mA cm^{-2} to 70% at 350 mA cm^{-2}. The densely packed Cu nanoneedles create significant diffusion resistance for CO as it moves from the Ag NPs, forcing CO to travel a longer path. This extended diffusion increased the likelihood of CO adsorption, promoting dimerization into C_{2+} products and thereby contributing to the enhanced CO_2RR performance.

Au-based

Similar to Ag, Au is particularly noted for its high selectivity towards CO, as it efficiently weakens CO_2 bonds and promotes the formation of CO intermediates. Bimetallic Au-Cu tandem catalysts have shown improved catalytic performance, with Au facilitating efficient CO production and Cu driving the subsequent C-C coupling, which is necessary to produce higher-value C_{2+} products. For example, Morales-Guio *et al.* employed electron-beam evaporation to arrange Au NPs onto polycrystalline copper foil (Au/Cu), creating tandem electrocatalysts[112]. These Au/Cu catalysts displayed superior CO_2 reduction activity towards C_{2+} alcohols compared to recently developed Cu-based bimetallic catalysts. The existence of Au NPs on the copper foil enhances the local concentration of CO on adjacent copper surfaces, which subsequently facilitates its reduction to C_{2+}. Notably, the Au/Cu catalysts demonstrated a selectivity for C_{2+} formation that was 100 times higher than that for CH_4 or CH_3OH at low overpotentials. Recently, Wang *et al.* used Au NPs of varying sizes and densities as a CO-producing component to boost CO_2 electroreduction into high-value chemicals[113]. They developed gold-copper oxide ($Au@Cu_2O$) tandem catalysts through a galvanic replacement reaction. Through modification of the Au NP size and the concentration of Au precursors, they explored the relationship between size and performance. The $Au@Cu_2O$ samples were designated as S-0.25, 0.5, and 2.0-$Au@Cu_2O$ for smaller Au NPs and L-0.25, 0.5, and 2.0-$Au@Cu_2O$ for larger Au NPs, reflecting the different sizes and concentrations of the Au precursors. The CO_2 reduction performance of L-0.5-Au@OD-Cu, S-0.5-Au@OD-Cu, S-2.0-Au@OD-Cu, and OD-Cu was assessed in a 1 M $KHCO_3$ using a flow cell. Our results showed that catalysts with smaller Au NPs exhibited more efficient CO_2 reduction reactions at a reduced overpotential compared to those with larger Au NPs and OD-Cu. Additionally, elevating the loading amount of Au NPs in $Au@Cu_2O$ catalysts led to a decline in the selectivity of C_{2+} products such as C_2H_4 and C_2H_6O, while enhancing the FE of n-propanol. Cao *et al.* synthesized tandem catalysts consisting of Au and cubic Cu_2O through a galvanic replacement reaction followed by pre-reduction using the LSV method[114]. Unlike bare Cu_2O, the Au_xCu_2O catalysts exhibited a shift in selectivity, with CO formation becoming more prominent. A significant increase in C_2H_4 selectivity was observed at potentials beyond -1.1 V *vs.* RHE. Among the catalysts, $Au_{0.02}Cu_2O$ achieved the highest FE for C_2H_4, reaching 24.4% with a total current density of approximately 5.7 mA cm^{-2} at -1.3 V *vs.* RHE, which was 2 to 2.5 times higher than that of the other Au_xCu_2O catalysts and five times greater than bare Cu_2O. This enhanced selectivity toward C_2H_4 was attributed to the optimal CO availability provided by Au atoms

and the improved C-C coupling facilitated by the synergistic effects of Cu^+ and Cu^0. Zhu *et al.* introduced an effective strategy for designing an epitaxial Au-Cu heterostructure aimed at enhancing the CO_2-to-C_{2+}[115]. The electrochemical CO_2 reduction was conducted in an H-cell using 0.1 M $KHCO_3$ as the electrolyte. The Au-Cu heterostructure demonstrated notable C_{2+} alcohols production, with an onset potential approximately 150 mV more positive than that of pure Cu and a conversion rate for CO_2 to C_{2+} alcohols that was about 2.5 times higher at -1.0 V *vs.* RHE [Figure 9A]. As illustrated in Figure 9B and C, the Au-Cu heterostructure not only produced more alcohol compared to Cu but also effectively suppressed hydrocarbon formation, achieving a superior ratio of C_{2+} alcohols/(CO + > 2e⁻ products). Furthermore, a dynamic restructuring was observed, where Au-Cu bimetals with phase separation transitioned into alloy-supported Au@Cu core-shell nanoclusters during electrocatalysis, forming Au@Cu-AuCu structures [Figure 9D]. A unique tandem mechanism was introduced, highlighting the accumulation of ˙CO as a key factor for maintaining the durability of C_{2+} alcohol production. Wei *et al.* applied a homo-nucleation method to decorate Au NPs onto the surface of Cu NWs[116]. Cu NWs are well-recognized for their significant aspect ratio with dense GBs, both of which have been shown to enhance electron transport and provide abundant active sites. They synthesized three tandem catalysts with varying Cu-to-Au mass ratios, labeled $Cu_{99.8}Au_{0.2}$, $Cu_{99.3}Au_{0.7}$, and $Cu_{96.7}Au_{3.3}$. Of these, $Cu_{99.3}Au_{0.7}$ demonstrated the best catalytic performance, achieving a $FE_{C_{2+}}$ of 65.3% at -1.25 V *vs.* RHE, which is a notable advancement over the pristine Cu NWs (39.7%). Among the C_{2+} products, selectivity was highest for C_2H_4 at 35%, followed by C_2H_6O at 19.1%. Zheng *et al.* developed tandem electrocatalysts based on Janus NPs to overcome the limitations posed by the spatial arrangement of different constituent components[117]. The Janus structure ensures optimal accessibility of the two linked metals, allowing the NPs to serve as dual-functional agents. Au-Cu Janus nanostructures (Au-Cu Janus NSs) were synthesized with N-oleyl-1,3-propanediamine (OPDA) as a capping agent. OPDA, with its amine group, is essential in inhibiting the surface oxidation of Cu NPs. To highlight the significance of OPDA in the formation of the Janus nanostructures, they also synthesized Au-Cu tandem catalysts using octadecylamine and oleylamine. When OPDA was replaced with other capping agents, the electrocatalysts did not display the Janus structure. The optimized Au-Cu Janus NSs exhibited selective CO_2 reduction towards C_{2+} products, achieving the highest total current density of nearly 1 Acm^{-2}, $FE_{C_{2+}}$ of 67% and a $j_{C_{2+}}$ of -0.29 A cm^{-2} at -0.75 V *vs.* RHE, outperforming both Au@Cu core-shell nanostructures and Cu NPs [Figure 9E-H]. The distinctive structure of the Au-Cu Janus NSs promoted CO spillovers from the Au sites to neighboring Cu, enhancing CO coverage and facilitating C-C coupling.

Molecular catalysts and single-atom catalysts based
Bimetallic systems integrating Cu with other CO-producing metals, including Au and Ag, have been extensively studied as electrocatalysts for C_{2+} production, as mentioned above[118-120]. However, a significant challenge with these catalysts is the potential for changes in composition and morphology during operation, which can alter both their physical and electronic properties. These variations complicate the insights into catalytic behavior and hinder the development of effective design principles to enhance catalytic performance. Consequently, substantial studies have concentrated on developing tandem catalysts that employ CO-producing molecular catalysts and single-atom catalysts (SACs). Liu *et al.* developed high-performance tandem catalysts composed of cobalt phthalocyanines (CoPc), acetylene black, and Cu_2O nanocrystals (Cu_2O NCs-C-CoPc)[121]. The electrocatalytic performance for C_{2+} products was evaluated using both H-cell and flow-cell systems. In the H-cell, Cu_2O NCs-C-Copc achieved a maximum FE for C_2H_4 of 58.4%, with a $j_{C_2H_4}$ of -29.74 mA cm^{-2} and durability of ten hours. When tested in the flow cell, the selectivity for C_2H_4 increased significantly to 70.3%, with a corresponding $j_{C_2H_4}$ of -226.18 mA cm^{-2}. Similarly, Kong *et al.* developed a tandem catalyst by integrating CoPc with a Cu GDE[122]. Initially, Cu was sputtered onto a polytetrafluoroethylene (PTFE) substrate, followed by spraying a CoPc-methanol solution onto the Cu GDE, creating the Cu-CoPc GDE. The optimized Cu-CoPc GDE exhibited excellent performance for CO_2
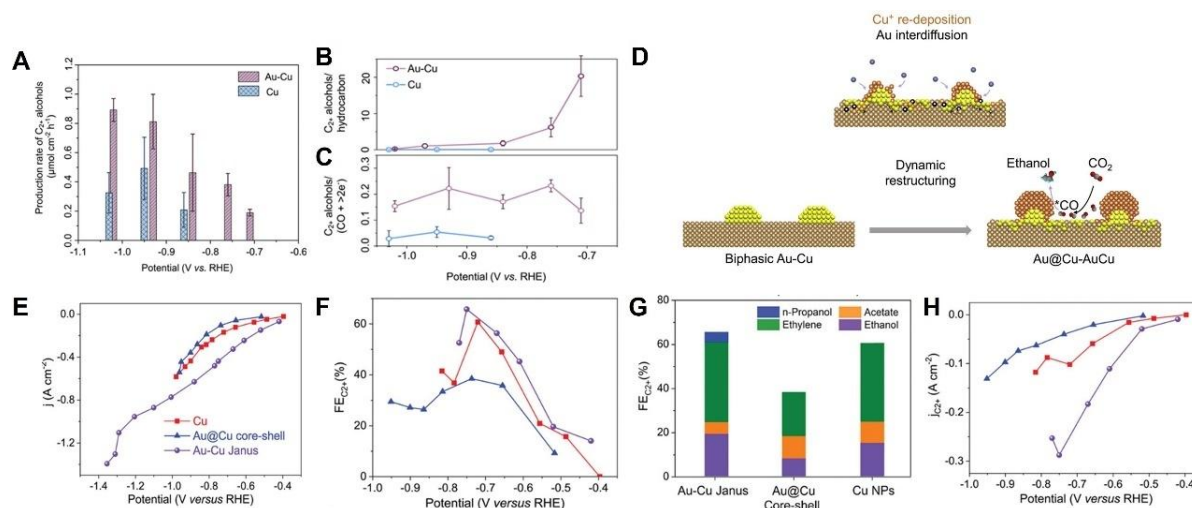
Figure 9. (A) Rate of C_{2+} production on Au-Cu and Cu electrodes; (B) Dependence of the molar ratio of C_{2+} alcohols to hydrocarbons and of (C) alcohols to (CO + > 2e⁻ products) on Au-Cu and Cu as a function of potential; (D) Diagram depicting phase transformation and structural reconstruction of Au-Cu during the CO_2RR process. This figure is quoted with permission from Zhu *et al.* Copyright (2022) Elsevier[115]; (E) Total current density of Cu, Au@Cu core-shell, and Au-Cu Janus electrocatalysts; (F) FE_{C2+} of three different catalysts. (G) Comparison of optimal FE_{C2+} obtained by using Au@Cu core-shell, Au-Cu Janus, and Cu NPs; (H) j_{C2+} of Au@Cu core-shell, Au-Cu Janus, and Cu NPs. This figure is quoted with permission from Zheng *et al.* Copyright (2022) John Wiley and Sons[117]. FE: Faradaic efficiency.

conversion to C_{2+} products, resulting from the high *CO coverage facilitated by the CO-producing CoPc. Specifically, the Cu-CoPc GDE achieved a FE of 82% for C_{2+} products at an applied current density of 480 mA cm⁻², which is 1.8 times higher than that of the Cu GDE alone. Min *et al.* utilized metal porphyrins, recognized for their efficiency in CO_2 adsorption and *CO intermediate formation[123]. Using a liquid-phase approach, they developed self-supporting tandem catalysts by modifying a cuprous oxide NW array supported on copper mesh decorated with cobalt(II) tetraphenylporphyrin (CoTPP) molecules, resulting in the CoTPP-Cu_2O@CM catalyst [Figure 10A]. The optimized CoTPP-Cu_2O@CM catalyst demonstrated enhanced C_{2+} selectivity in an H-cell, achieving a FE of 73.2% for C_{2+} products and a current density of -52.9 mA cm⁻² at -1.1 V *vs.* RHE, surpassing the performance of recently reported Cu-based catalysts [Figure 10B and C]. Furthermore, CoTPP-Cu_2O@CM catalyst exhibited long-term durability of about 14 h without significant change in FE_{C2H4} and current density [Figure 10D].

SACs are a unique type of catalyst with well-defined coordination and distinct electronic structures[124]. Among the SACs, Ni SACs demonstrate excellent conversion of CO_2 to CO, making them particularly appealing for use in tandem catalysts. For instance, Zhang *et al.* developed a highly C_2H_4 selectivity tandem catalyst by simply mixing colloidal Cu NPs and Ni SACs (Cu NPs/Ni-N-C)[125]. The colloidal Cu NPs were first synthesized using Tetradecylphosphonic acid (TDPA) as a capping agent, allowing precise control over the size and shape of the NPs. The optimized Cu NPs/Ni-N-C catalyst exhibited excellent performance for C_2H_4 production, achieving a FE of 14.52%, a j_{C2H4} of -1.67 mA cm⁻², and a C_2H_4/CH_4 ratio of 20.1 at -0.9 V *vs.* RHE. Zhang *et al.* developed CuO/Ni tandem catalysts, composed of CuO and Ni SAs, aimed at enhancing C_{2+} production[126]. They investigated three strategies for fabricating tandem catalytic electrodes: layer-by-layer spraying, adjacent nanostructures, and physical mixing. Among these, the adjacent nanostructure electrode demonstrated superior efficiency by promoting more effective CO generation at the Ni sites, thereby increasing the local CO concentration near the Cu sites and enhancing C_{2+} product formation. Consequently, the CuO/Ni SA tandem catalyst attained an impressive j_{C2+} of 1,220.8 mA cm⁻², along with a high FE for C_{2+} products at 81.4%. Among the FE_{C2+}, FE towards C_2H_4 resulted in 54.1% and
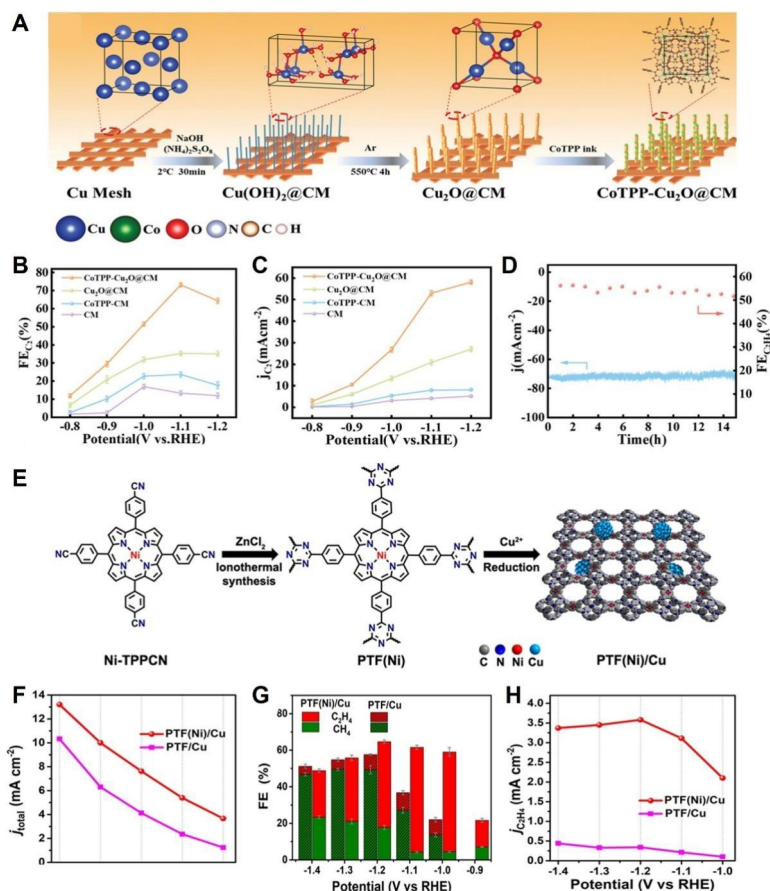
Figure 10. (A) Fabrication of CoTPP-Cu₂O@CM NWs array; (B) FE$_{C2+}$ of CoTPP-Cu₂O@CM, Cu₂O@CM, CoTPP-CM, and Cu mesh; (C) j$_{C2+}$ of CoTPP-Cu₂O@CM, Cu₂O@CM, CoTPP-CM, and Cu mesh; (D) Stability test of CoTPP-Cu₂O@CM for 15 h. This figure is quoted with permission from Min *et al.* Copyright (2024) John Wiley and Sons[123]; (E) Graphic representation of PTF(Ni)/Cu; (F) Total current densities on PTF(Ni)/Cu and PTF/Cu catalysts; (G) FEs for the production of C₂H₄ and CH₄ on PTF(Ni)/Cu and PTF/Cu catalysts at different potentials; (H) j$_{C2H4}$ of PTF(Ni)/Cu. This figure is quoted with permission from Meng *et al.* Copyright (2021) John Wiley and Sons[128]. CoTPP: cobalt(II) tetraphenylporphyrin; PTF: porphyritic triazine framework.

28.8% for C₂H₆O. Additionally, Liu *et al.* developed tandem electrocatalysts featuring nickel SAs, which exhibited a wide potential window for CO generation when combined with copper (Ni SAC + Cu-R)[127]. To assess the function of Ni SACs, DFT calculations were conducted to compare the activation barriers for *OCCO formation, using Ag NPs and Nickel phthalocyanines as control references. To support their theoretical results, Ni SACs were synthesized through electrostatic self-assembly, while Cu catalysts were produced using a one-step wet chemical reduction method. The Ni SAC + Cu-R tandem catalysts were then prepared by thoroughly mixing Ni SAC and Cu-R. The CO₂ electroreduction performance was evaluated in a flow cell with 1M KHCO₃ solution. The Ni SAC + Cu-R catalysts showed significantly improved performance compared to individual Ni SAC and Cu-R catalysts, achieving a j$_{C2H4}$ of ~370 mA cm⁻² for C₂H₄ with a FE of ~62% and a stability of approximately 14 h at a current density of 500 mA cm⁻². Meng *et al.* developed a facile approach to construct a tandem catalyst composed of Cu NPs on a porphyritic triazine framework anchored with atomically isolated nickel-nitrogen sites [PTF(Ni)][128]. PTF(Ni), with abundant porosity, was fabricated, and Cu NPs were embedded through a reduction reaction step, resulting in PTF(Ni)/Cu [Figure 10E]. H-type cells with the mixed electrolyte of 0.1 M KHCO₃ and 0.1 M KCl saturated with CO₂ were utilized to evaluate the catalytic performance of the catalysts. Compared to PTF/Cu, PTF(Ni)/Cu demonstrated outstanding performance, achieving a peak FE$_{C2H4}$ of 57.3% and a j$_{C2H4}$ of

3.1 mA cm^{-2} at -1.1 V *vs.* RHE [Figure 10F-H]. This suggests that the atomically dispersed Ni sites in PTF(Ni)/Cu serve a vital function in increasing the selectivity for C_2H_4 by facilitating the generation of CO, causing an increased accumulation of *CO intermediate. Similarly, Chen *et al.* encapsulated Cu NPs in mesoporous carbon (CMK-8) with doped atomic Ni-N$_4$ moieties, resulting in a-Ni/Cu-NP@CMK[129]. Electrochemical tests indicate that a-Ni/Cu-NP@CMK exhibits remarkable selectivity for C_2H_4, achieving a FE_{C2H4} of 72.3% at a notable current density of 406.1 mA cm^{-2} when operated in a flow cell under neutral conditions. Furthermore, when measured using a membrane electrode assembly (MEA) cell, a-Ni/Cu-NP@CMK demonstrated excellent stability of over 30 h under the 200 mA cm^{-2} and a FE_{C2H4} of 63% at -2.8 V *vs.* RHE. Furthermore, the optimized a-Ni/Cu-NP@CMK exhibited superior energy efficiency for C_2H_4 production of about 28.3%. The authors suggested that the abundance of CO molecules around the active sites and the hydrophobic environments contributed to the high performance of a-Ni/Cu-NP@CMK in C_2H_4 production.

Non-Cu-based catalysts

Cu is the primary metal known to produce C_{2+} products; however, recent studies indicate that several non-Cu-based catalysts can also generate C_{2+} products with careful design. Paris *et al.* fabricated a novel Ni$_3$Al deposited glassy carbon electrode by drop-casting and furnace reduction process[130]. The as-synthesized electrode successfully converted CO_2 into C_{2+} and C_{3+} products for the first time, with the maximum FEs for ethane, ethylene, and 1-propanol reaching 1.7%, 0.4%, and 1.9 ± 0.3%, respectively. Torelli *et al.* synthesized several Ni-Ga alloys with distinct phases (NiGa, Ni$_3$Ga, and Ni$_5$Ga$_3$), which can convert CO_2 to C_{2+} at low overpotentials[131]. The Ni$_5$Ga$_3$ alloy achieved a FE of 1.3% for C_2H_6 at -0.48 V vs RHE, whereas Cu-based catalysts only produced CH_4 at the same low overpotential. Recently, Ding *et al.* reported Sn-based electrocatalysts with superior catalytic performance for CO_2 electroreduction to ethanol[132]. Sn-based electrocatalyst is composed of SnS$_2$ NSs and Sn SACs (SnS$_2$/Sn$_1$-O$_3$G). The electrocatalytic performance for CO_2RR was evaluated in an H-cell with 0.5 M KHCO$_3$ as the electrolyte. SnS$_2$/Sn$_1$-O$_3$G exhibited excellent selectivity toward ethanol, with a FE above 70% over a wide potential window, reaching a maximum FE of 82.5% for ethanol at -0.9 V *vs.* RHE. Furthermore, it demonstrated exceptional long-term stability, maintaining 97% of its initial activity after 100 h. This outstanding performance is primarily attributed to the dual active centers of Sn and O atoms on Sn$_1$-O$_3$G, which facilitate the formyl-bicarbonate coupling pathway, thereby enhancing selectivity toward ethanol.

ELECTROCHEMICAL CELLS FOR CO$_2$RR

In addition to catalysts, electrochemical cell design is another crucial factor affecting the CO_2 reduction. There are three types of reactors for the eCO$_2$RR conversion, including an H-type cell, flow cell and MEA cell, as shown in Figure 11[133]. Notable advancements have been made in the design and fabrication of electrolytic cells to attain highly efficient C_{2+} production. Here, we briefly explore the advantages and disadvantages of each electrolytic cell with examples.

H-type cells

H-type cells are widely utilized for lab-based experiments due to their simple assembly, ease of operation, and low cost. These have distinct cathode and anode chambers, separated by an ion-exchange membrane. During the reaction, CO_2 gas is bubbled through the aqueous catholyte, where dissolved CO_2 molecules are adsorbed onto the electrocatalyst surfaces and subsequently reduced[134,135]. However, a key limitation of H-type cells is the poor dissolution of CO_2 in aqueous electrolytes, reaching only 0.034 M under ambient conditions, which restricts CO_2 reduction current densities to below 100 mA cm^{-2}. Additionally, other inherent limitations, such as a small electrode surface area and a significant interelectrode distance, hinder the ability to meet the increasing demands for C_{2+} product generation[136-138]. Consequently, H-type cells
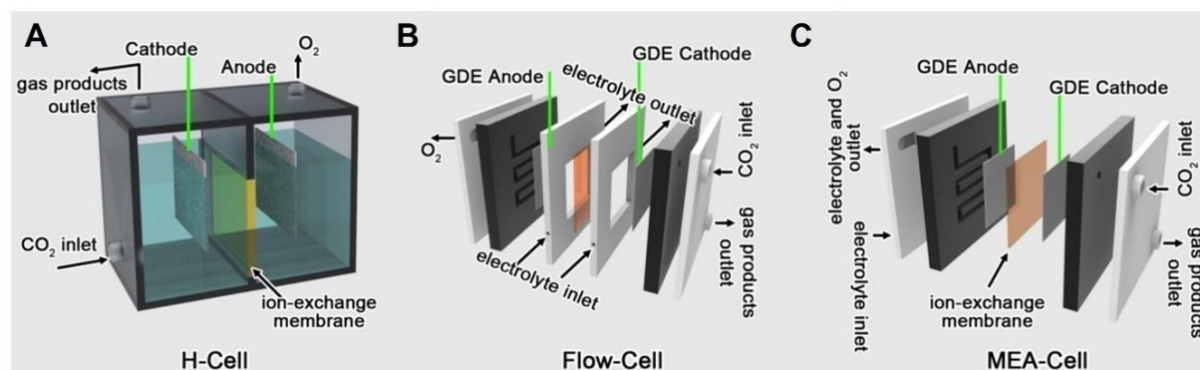
Figure 11. (A) H-cell, (B) flow-cell, and (C) MEA-cell configurations for eCO$_2$RR. This figure is quoted with permission from She *et al.* Copyright (2022) John Wiley and Sons[133]. eCO$_2$RR: electrocatalytic CO$_2$ reduction reaction; MEA: membrane electrode assembly.

generally show low selectivity for C$_{2+}$ products. As an example, Kas *et al.* described a Cu foil with a supreme C$_2$H$_4$ FE of 33% at -1.1 V *vs.* RHE, while Zhang *et al.* documented Cu monolayer-modified Pd NCs electrocatalysts, achieving an ethanol FE of 20.4% at -0.46 V *vs.* RHE, primarily due to intense competition from HER[27,139].

GDE flow cells

Flow cells have been introduced to address the limitations of H-type cells. A standard flow cell comprises five primary components: flow field plates, support plates, ion exchange membranes, cathode and anode GDEs, and electrolytes[140]. Catholyte and anolyte are continuously circulated through the peristaltic pump. Moreover, CO$_2$ gas directly feeds into the cathode, significantly improving mass transport and boosting production rates[141-144]. As a result, the thermodynamics and kinetics of CO$_2$RR in flow cells differ significantly from those in traditional H-type cells, making flow cells more favorable for large-scale commercial applications[145-147]. An important aspect of flow cells is the GDEs, which improve CO$_2$RR performance by forming porous hydrophobic channels that facilitate the transport of CO$_2$ gas to the catalyst-electrolyte interface, thus creating a stable gas-solid-liquid three-phase environment[135,147,148]. GDEs primarily comprise three layers: the GDL, the current collector (CC), and the CL. The GDL offers numerous porous channels for efficient CO$_2$ transport and serves as a stable support for the catalyst[149]. The CC enables efficient electron transport and reduces internal resistance, while the CL serves as the primary reaction zone, where the gas-solid-liquid three-phase interface is established and CO$_2$RR primarily occurs[150]. Owing to these advantages, the selectivity for C$_{2+}$ is higher than for an H-cell. For example, Wang *et al.* developed a single-atom Ga catalyst anchored on F-doped Cu$_2$O mesoporous catalyst (Ga$_1$-F/Cu$_2$O), and assessed its CO$_2$RR performance in a flow cell, as depicted in Figure 12A[151]. Using flow cells, the Ga$_1$-F/Cu$_2$O demonstrated a maximum FE of 72.8 ± 3.2% for C$_{2+}$ with a C$_{2+}$ products yield rate of 1.36 mmol h^{-1} cm^{-2} at a current density of 600 mA cm^{-2} [Figure 12B and C]. Furthermore, the electrochemical CO$_2$ reduction (ECR) performance of 5% B-Cu$_x$O was tested in both H-type and flow cells [Figure 12D and E][152]. In the H-type cell, the optimal FE for C$_{2+}$ products was 48.44% at -1.0 V *vs.* RHE. On the contrary, the FE for C$_{2+}$ products increased to 55.73% under the same potential in the flow cell. This significant enhancement in performance with the flow cell is ascribed to better CO$_2$ diffusion and the suppression of HER, mainly due to the localized gas-electrolyte-catalyst triple-interface configuration. Alkaline electrolytes are commonly used in flow cells due to their effectiveness in facilitating CO$_2$RR. For example, electrolytes such as KOH provide abundant OH$^-$ ions, which enhance electron transfer to CO$_2$ molecules, reducing the energy barrier for CO$_2$RR and decreasing the overpotential required for CO$_2$ reduction. Furthermore, the high concentration of OH$^-$ ions reduces H* availability, effectively suppressing HER. However, a major drawback of alkaline electrolytes is their reaction with CO$_2$ gas to form bicarbonate,
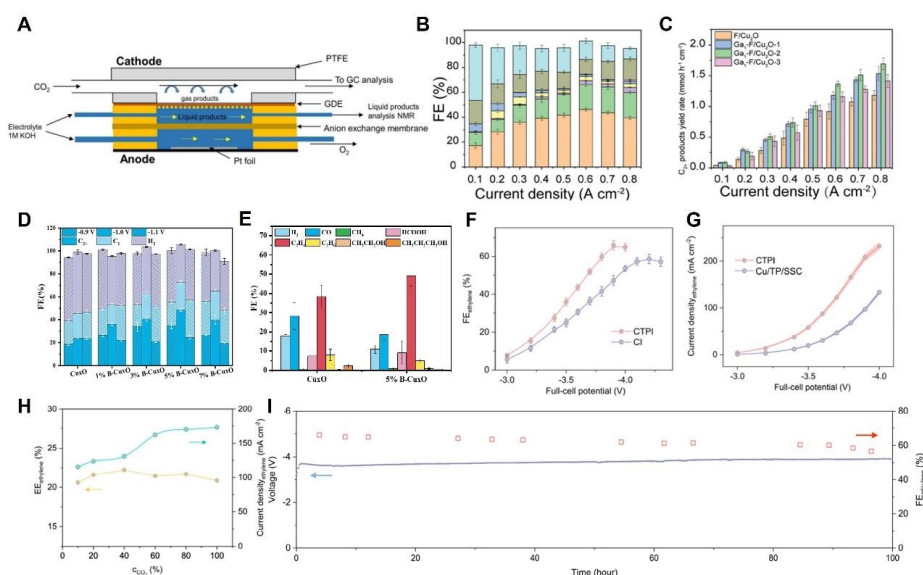
Figure 12. (A) Flow cell used in electrochemical tests; (B) FE values of CO_2RR products on Ga_1-F/Cu_2O-2; (C) C_{2+} product yield rates at different applied current densities of F/Cu_2O, Ga_1-F/Cu_2O-1, Ga_1-F/Cu_2O-2, and Ga_1-F/Cu_2O-3. This figure is quoted with permission from Wang *et al.* Copyright (2024) John Wiley and Sons[151]; (D) FEs of H_2, C_1, and C_{2+} on Cu_xO and various B-Cu_xO samples measured with H-cell; (E) FEs of CO_2RR products on Cu_xO and 5% B-Cu_xO measured with flow cells. This figure is quoted with permission from Yang *et al.* Copyright (2024) Elsevier[152]; (F) FE_{C2H4} for the 3D CTPI (tetrahydro-phenanthrolinium/SSC-modified Cu NPs on Cu/PTFE) as well as 3D CI (SSC modified-Cu NPs on Cu/PTFE); (G) j_{C2H4} for 3D CTPI (tetrahydro-phenanthrolinium/SSC-modified Cu NPs on Cu/PTFE) and 3D CI (SSC modified-Cu NPs on Cu/PTFE); (H) Full-cell energy efficiency and j_{C2H4} with different CO_2 concentrations; (I) Durability measurement of 3D CTPI catalyst at 220 mA cm^{-2}. This figure is quoted with permission from Ozden *et al.* Copyright (2020) American Chemical Society[166]. FE: Faradaic efficiency; CO_2RR: CO_2 reduction reaction; NPs: nanoparticles; 3D: three-dimensional; PTFE: polytetrafluoroethylene; CTPI: catalyst/tetrahydro-phenanthrolinium/ionomer; SSC: short-side-chain.

which can block CO_2 transport channels and reduce CO_2RR efficiency[153]. To overcome these challenges, acidic electrolytes have been explored as a potential alternative. Acidic electrolytes, characterized by their high concentration of H^+ ions, prevent the reaction between CO_2 and the electrolyte, thereby reducing carbonate formation and mitigating salt precipitation[154]. This results in improved single-pass carbon efficiency (SPCE). Furthermore, the abundance of protons in acidic electrolytes enhances the adsorption and activation of CO_2 molecules on the electrode surface, accelerating the CO_2RR reaction rate and enhancing current density.

For example, Wang *et al.* reported a Pd-doped Cu/Cu_2O catalyst designed to enhance C-C coupling for improved C_{2+} product formation[155]. eCO_2RR tests of the Pd-doped Cu/Cu_2O catalyst were conducted in an acidic electrolyte (pH = 2). The optimized catalyst achieved a maximum FE of 64.0% for C_{2+} products, with a corresponding C_{2+} partial current density of 407.1 mA cm^{-2} at -2.18 V *vs.* RHE. Additionally, it exhibited a high single-pass CO_2 conversion efficiency of 73.2% and excellent electrochemical stability, maintaining performance for approximately 150 h.

MEA cells
MEA cells are a promising reactor design for industrial-scale CO_2 reduction. They are double-electrode configurations that do not require a reference electrode[156]. Instead of using potential control as in H-type cells, MEA cells are regulated by current or voltage. Their configuration is similar to that of flow cells, but with a key distinction: in MEA cells, the anode and cathode are positioned directly on opposite sides of an ion-exchange membrane, forming a compact, sandwich-like structure[157-159]. This membrane promotes the transfer of ions and circumvents products' crossover. Additionally, this cell design allows CO_2 to be

continuously delivered to the cathode and the electrolyte to be supplied to the anode, while eliminating the need for a separate catholyte at the cathode[133,160,161]. CO_2 can be delivered to the cathode in two ways: by pumping a CO_2-saturated solution into the cathodic compartment or by directly introducing CO_2 gas, with or without added humidity[162]. This approach increases the concentration of reactants at the catalyst surface, resulting in higher reaction rates[163-165]. As a result, the MEA configuration simplifies the overall structure of the electrolytic cell, reduces mass and electron transfer resistance, and enhances energy efficiency, thereby positioning it as a more practical alternative for industrial applications. For example, Ozden *et al.* fabricated high-performance electrodes with a tetrahydro-phenanthrolinium-modified hierarchical adlayer with Cu NPs[166]. The As-fabricated electrode achieved 66% of C_2H_4 FE at partial current densities of over 200 mA cm^{-2} and full cell energy efficiency of 21% in an MEA cell [Figure 12F-H]. Moreover, the electrolysis system showed remarkably superior durability of over 100 h of continuous operation at a cell voltage of 3.8 V [Figure 12I]. Despite their potential, MEAs in CO_2RR still face several unresolved challenges, including carbonate salt precipitation, cathode flooding, and the crossover of reaction products. Addressing these issues remains critical for the development of stable and efficient MEA systems.

Microfluidic electrolytic cells
Microfluidic electrolytic cells (MECs) consist of two chambers for electrolyte flow, separated by GDEs. The reaction products are carried out of the electrocatalytic cells along with the flowing liquid electrolyte. MECs provide several benefits, including (1) the ability to conveniently and rapidly adjust operating conditions and (2) a simple and efficient process for collecting final products[146]. These features make MECs highly suitable for evaluating catalyst performance under various conditions. However, the lack of separation between the anode and cathode allows products to migrate in opposite directions under electromagnetic forces, potentially leading to the oxidation of final products at the anode. This can reduce product selectivity and decrease the overall energy efficiency of the system.

Solid-state electrolytes electrolyzer
Solid-state electrolyzers represent a novel class of electrochemical CO_2 cells, ideal for producing liquid products with high purity and concentration and have recently attracted significant research attention. In these systems, the cathode and anode are separated by an anion exchange membrane (AEM) and a cation exchange membrane (CEM), respectively, while a porous solid electrolyte layer with various functional groups serves as an intermediate channel[167,168]. The ions generated during the CO_2RR process recombine with protons in this intermediate channel to form the desired liquid product, which is then collected by N_2 purging. While this design facilitates easy separation of the liquid products, the inclusion of the solid electrolyte layer introduces additional resistance, leading to a substantial increase in the overall cell voltage.

IN-SITU /OPERANDO CHARACTERIZATION TECHNIQUES
Cu-based catalysts undergo changes in their oxidation state during the CO_2RR, making catalyst characterization and performance evaluation quite challenging. To investigate the CO_2RR mechanism, *ex-situ* techniques have traditionally been used; however, the information gathered from these methods is limited. To address these limitations, *in-situ*/operando characterization techniques have gained significant attention. These methods offer advantages such as real-time monitoring, higher realism, and greater accuracy, making them more effective for elucidating reaction mechanisms and studying the structure-reactivity/selectivity relationships of catalysts. *In-situ*/operando techniques are designed to capture precise data under actual reaction conditions, enabling the study of dynamic catalyst structures across multiple time–space scales. This section will focus on key *in-situ*/operando techniques, including infrared, Raman, and X-ray absorption spectroscopy (XAS).

In-situ/operando Fourier transform infrared spectroscopy

Fourier Transform Infrared (FT-IR) spectroscopy utilizes infrared light to induce molecular vibrations, enabling the identification of chemical compounds through their unique infrared absorption profiles. These absorption patterns result from dipole moment changes caused by molecular vibrations or rotations within a solution. In *in-situ* FT-IR applications, two primary approaches are used: thin-layer mode and attenuated total reflection (ATR) mode[169]. Thin-layer mode offers simplicity in design and operation but is less sensitive than ATR mode. ATR mode, while more complex and requiring precise optical alignment, minimizes interference from the bulk solution, producing spectra with higher clarity and signal-to-noise ratios. *In-situ*/Operando FT-IR is a highly effective tool for examining CO_2RR, as it directly observes reaction intermediates and provides detailed insights into their adsorption configurations [Figure 13A][170,171]. This technique also helps uncover the chemical properties of the system and facilitates the structural analysis of catalysts. By carefully choosing measurement methods, researchers can better understand chemical composition, phase transitions, and reaction intermediates, deepening their knowledge of how catalyst structures influence performance[172-174].

In-situ/operando Raman spectroscopy

In-situ/operando Raman spectroscopy is operated in confocal mode within a chemical reaction cell setup [Figure 13B]. By utilizing this technique to track changes in the appearance, intensity, or disappearance of specific Raman peaks, it is possible to observe shifts in oxidation states and infer the underlying reaction mechanism[175]. A significant challenge in *in-situ* Raman measurements is enhancing detection limits without compromising the electrochemical responses in liquid electrolytes. Given the weak signals in conventional Raman spectroscopy, surface-enhanced Raman spectroscopy (SERS) was developed to offer higher sensitivity and reduce interference from water when detecting surface metal species[176,177]. In general, Raman scattering from molecules adsorbed onto the rough surfaces of plasmonic metal nanostructures is significantly enhanced. However, SERS is constrained by the type and morphology of the material, with effective enhancement occurring only with specific metals and rough surfaces[178]. Moreover, the technique has limited spatial resolution because of the excitation wavelength. To address these challenges, shell-isolated NPs enhanced Raman spectroscopy (SHINERS) has been introduced as an alternative. SHINERS techniques employ chemically inert and ultra-thin SiO_2 or Al_2O_3 shells to isolate Au or Ag NPs, which can eliminate problems related to impurity interference, and signal deviation in the SERS field[166].

While *in-situ*/operando Raman spectroscopy has made significant advancements in the field of CO_2RR, several challenges persist: (1) the liquid flow can interfere with detection, and (2) high current densities may affect the Raman signal.

In-situ/operando XAS

XAS is also an effective technique for investigating the electronic structure and coordination environment of materials[179]. It is generally divided into two regions: X-ray absorption near-edge structure, which provides insights into the electronic structure of atomic orbitals, such as the oxidation state of the element and symmetry, and extended X-ray absorption fine structure, which helps analyze the local coordination environment, including the coordination number, coordinating elements, and interatomic distances. Electrochemical reactions typically involve chemical adsorption and electron transfer, which lead to structural and oxidation state changes in catalysts. These changes are reversible and challenging to track accurately with ex-situ characterization methods. In contrast, *in-situ*/operando XAS offers the advantage of precisely detecting changes in the oxidation state and local structure of catalyst elements, monitoring catalyst reconfiguration during electrolysis, and identifying the active sites of the catalysts [Figure 13C][180].
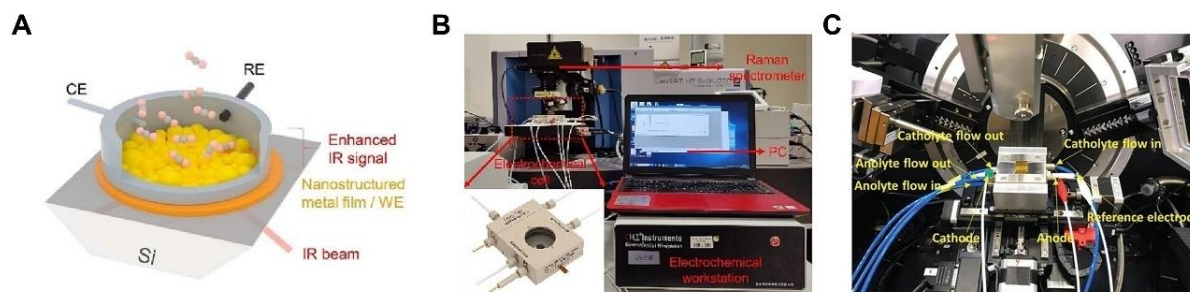
Figure 13. Schematic illustrations of *in-situ/*operando techniques in CO_2RR. (A) *In-situ* ATR-FT-IR spectroscopy; (B) *In-situ/*operando Raman spectroscopy. This figure is quoted with permission from Dutta *et al.* Copyright (2023) Elsevier[175]. (C) *In-situ/*operando XAS. This figure is quoted with permission from Song *et al.* Copyright (2023) John Wiley and Sons[180]. CO_2RR: CO_2 reduction reaction; XAS: X-ray absorption spectroscopy; ATR-FT-IR: attenuated total reflectance Fourier-transform infrared.

CONCLUSION AND FUTURE PERSPECTIVES

Utilizing CO_2 reduction in combination with renewable energy sources to generate high-energy density C_{2+} hydrocarbons presents a promising approach for advancing a sustainable society. In this review, we have provided an overview of the latest developments that facilitate greater selectivity and higher production rates for C_{2+} products, through methods such as catalyst tuning and electrochemical reactor design. For the catalyst-tuning, we divided into four main strategies including defect engineering, nanostructure design, surface modifications, and tandem catalysis with various CO-producing metals and provided a detailed examination of the prevailing methods used. Following this, we explored the design of electrochemical reactors, covering the commonly used H-cell, flow cell, and MEA cell, along with their key characteristics, advantages, and disadvantages. Despite the progress made, achieving low-cost and high-efficiency CO_2 reduction to high-value products remains a significant challenge. Therefore, we conclude with a discussion on future research directions and the key obstacles to be addressed: (1) Many advanced and efficient electrocatalysts possess specialized nanostructures and are typically produced through multi-step processes on a laboratory scale. However, scaling up these techniques with conventional laboratory methods is often impractical. Consequently, there is an urgent need for innovative technologies to enable the large-scale synthesis of Cu-based catalysts with high selectivity, activity, and stability, which will involve careful selection of electrochemical conditions for industrial-scale CO_2 electrocatalytic reduction; (2) Achieving industrial feasibility for CO_2 reduction technology requires electrocatalysts to maintain stability for tens of thousands of operational hours[181]. However, Cu-based catalysts face significant stability issues, particularly in aqueous electrolytes, where issues such as high atom mobility, particle aggregation, and structural degradation often restrict their lifespan to less than 100 h under CO_2RR conditions[182]. Consequently, achieving long-term stability with Cu-based catalysts remains a key challenge. Research into effective strategies for anchoring Cu-based catalysts on specific supports with strong metal-support interactions is necessary to preserve their structure and enhance long-term durability; (3) Cu-based electrocatalysts have demonstrated considerable potential for CO_2RR, especially in facilitating the production of valuable C_{2+} products. Despite extensive research aimed at improving the selectivity of Cu-based catalysts for C_{2+} products, their performance remains limited. Therefore, the rational design of novel and efficient electrocatalysts with unique electronic structures and catalytic properties is essential. High-entropy alloys (HEAs), which consist of multiple metal elements, have emerged as promising candidates for CO_2RR due to their tunable surface compositions and high configurational entropy. Despite their theoretical advantages, experimental evidence demonstrating the performance of Cu-based HEAs in CO_2RR remains limited, with most studies confined to computational simulations. Experimental validation of Cu-based HEAs for electrochemical CO_2 reduction to C_{2+} products would not only bridge the gap between computational studies and practical applications but also pave the way for the design of next-generation catalysts with

enhanced C_{2+} efficiency and selectivity; (4) From a catalyst perspective, a deeper understanding of the CO_2-to-C_{2+} reaction mechanisms is still needed. Advancing *in situ* and in operando characterization techniques to study the dynamic behavior of Cu-based catalysts, key intermediates, interfaces, and microenvironments during CO_2RR is crucial for identifying the intrinsic factors that promote C_{2+} formation; (5) At present, electrochemical cells such as flow cells and MEAs face challenges related to long-term stability. Key issues include catalyst detachment from the GDL and electrolyte flooding or salt buildup within the GDL. Addressing these problems requires the advancement of innovative binders with strong mechanical strength and durability, and the precise design of GDE structures that maintain stability at high current densities[183]; (6) Finally, innovative electrode and reactor designs are needed to increase electrochemical CO_2 reduction production rates to commercially viable levels (> 200 mA cm^{-2}). However, significant discrepancies in electrocatalytic performance often arise when transitioning from half-cell studies to full-cell applications. To bridge this gap and move eCO_2RR from lab-scale tests to practical applications, systematic research is essential to better align the performance of half-cell and full-cell systems.

In summary, while notable advancements have been made, there is still considerable work to be done in developing high-performance CO_2-to-C_{2+} systems. Continued efforts will be crucial in paving the way toward a carbon-neutral future.

DECLARATIONS

Authors' contributions
Proposed the topic of this review: Kim, S. Y.
Prepared the manuscript: Ma, J.

Availability of data and materials
Not applicable.

Conflicts of interest
Kim, S. Y. is an Associate Editor of the journal *Energy Materials* and was not involved in any steps of editorial processing, notably including reviewer selection, manuscript handling and decision-making. The other author declares that there are no conflicts of interest.

Ethical approval and consent to participate
Not applicable.

Consent for publication
Not applicable.

REFERENCES
1.   Parson, E. A.; Keith, D. W. Fossil fuels without CO_2 emissions. *Science* **1998**, *282*, 1053-4. DOI
2.   Fan, X.; Rabelo, M.; Hu, Y.; Khokhar, M. Q.; Kim, Y.; Yi, J. Factors affecting the performance of HJT silicon solar cells in the intrinsic and emitter layers: a review. *Trans. Electr. Electron. Mater.* **2023**, *24*, 123-31. DOI

3.   Cho, J.; Kim, B.; Ryu, S.; et al. Multifunctional green solvent for efficient perovskite solar cells. *Electron. Mater. Lett.* **2023**, *19*, 462-70. DOI

4.   Muradov, N. Low to near-zero CO_2 production of hydrogen from fossil fuels: status and perspectives. *Int. J. Hydrogen. Energy.* **2017**, *42*, 14058-88. DOI

5.   Detz, R. J.; Ferchaud, C. J.; Kalkman, A. J.; et al. Electrochemical CO_2 conversion technologies: state-of-the-art and future perspectives. *Sustainable. Energy. Fuels.* **2023**, *7*, 5445-72. DOI

6.   Das, T. K.; Jesionek, M.; Çelik, Y.; Poater, A. Catalytic polymer nanocomposites for environmental remediation of wastewater. *Sci. Total. Environ.* **2023**, *901*, 165772. DOI PubMed

7.   Khokhar, M. Q.; Yousuf, H.; Jeong, S.; et al. A review on p-type tunnel oxide passivated contact (TOPCon) solar cell. *Trans. Electr. Electron. Mater.* **2023**, *24*, 169-77. DOI

8.   Anwar, M. N.; Fayyaz, A.; Sohail, N. F.; et al. CO_2 utilization: turning greenhouse gas into fuels and valuable products. *J. Environ. Manage.* **2020**, *260*, 110059. DOI

9.   Peter, S. C. Reduction of CO_2 to chemicals and fuels: a solution to global warming and energy crisis. *ACS. Energy. Lett.* **2018**, *3*, 1557-61. DOI

10. Song, Q.; Ma, R.; Liu, P.; Zhang, K.; He, L. Recent progress in CO_2 conversion into organic chemicals by molecular catalysis. *Green. Chem.* **2023**, *25*, 6538-60. DOI

11. Xia, Q.; Yang, J.; Hu, L.; Zhao, H.; Lu, Y. Biotransforming CO_2 into valuable chemicals. *J. Clean. Prod.* **2024**, *434*, 140185. DOI

12. Fang, S.; Rahaman, M.; Bharti, J.; et al. Photocatalytic CO_2 reduction. *Nat. Rev. Methods. Primers.* **2023**, *3*, 61. DOI

13. Alkhatib, I. I.; Garlisi, C.; Pagliaro, M.; Al-ali, K.; Palmisano, G. Metal-organic frameworks for photocatalytic CO_2 reduction under visible radiation: a review of strategies and applications. *Catal. Today.* **2020**, *340*, 209-24. DOI

14. Ye, W.; Guo, X.; Ma, T. A review on electrochemical synthesized copper-based catalysts for electrochemical reduction of CO_2 to C_{2+} products. *Chem. Eng. J.* **2021**, *414*, 128825. DOI

15. Birdja, Y. Y.; Pérez-gallent, E.; Figueiredo, M. C.; Göttle, A. J.; Calle-vallejo, F.; Koper, M. T. M. Advances and challenges in understanding the electrocatalytic conversion of carbon dioxide to fuels. *Nat. Energy.* **2019**, *4*, 732-45. DOI

16. Liu, X.; Jiao, Y.; Zheng, Y.; Jaroniec, M.; Qiao, S. Z. Building Up a picture of the electrocatalytic nitrogen reduction activity of transition metal single-atom catalysts. *J. Am. Chem. Soc.* **2019**, *141*, 9664-72. DOI

17. Cho, J. H.; Lee, C.; Hong, S. H.; et al. Transition metal ion doping on ZIF-8 enhances the electrochemical CO_2 reduction reaction. *Adv. Mater.* **2023**, *35*, 2208224. DOI

18. Cho, J. H.; Ma, J.; Lee, C.; et al. Crystallographically vacancy-induced MOF nanosheet as rational single-atom support for accelerating CO_2 electroreduction to CO. *Carbon. Energy.* **2024**, *6*, e510. DOI

19. Nitopi, S.; Bertheussen, E.; Scott, S. B.; et al. Progress and perspectives of electrochemical CO_2 reduction on copper in aqueous electrolyte. *Chem. Rev.* **2019**, *119*, 7610-72. DOI

20. Al-rowaili, F. N.; Jamal, A.; Ba, S. M. S.; Rana, A. A review on recent advances for electrochemical reduction of carbon dioxide to methanol using metal-organic framework (MOF) and Non-MOF catalysts: challenges and future prospects. *ACS. Sustainable. Chem. Eng.* **2018**, *6*, 15895-914. DOI

21. Wu, J.; Zhou, X. Catalytic conversion of CO_2 to value added fuels: current status, challenges, and future directions. *Chin. J. Catal.* **2016**, *37*, 999-1015. DOI

22. Kibria, M. G.; Edwards, J. P.; Gabardo, C. M.; et al. Electrochemical CO_2 reduction into chemical feedstocks: from mechanistic electrocatalysis models to system design. *Adv. Mater.* **2019**, *31*, e1807166. DOI

23. Liang, C.; Kim, B.; Yang, S.; et al. High efficiency electrochemical reduction of CO_2 beyond the two-electron transfer pathway on grain boundary rich ultra-small SnO_2 nanoparticles. *J. Mater. Chem. A.* **2018**, *6*, 10313-9. DOI

24. Hussain, M. S.; Ahmed, S.; Irshad, M.; et al. Recent engineering strategies for enhancing C_{2+} product formation in copper-catalyzed CO_2 electroreduction. *Nano. Mater. Sci.* **2024**,. DOI

25. Ma, M.; Djanashvili, K.; Smith, W. A. Selective electrochemical reduction of CO_2 to CO on CuO-derived Cu nanowires. *Phys. Chem. Chem. Phys.* **2015**, *17*, 20861-7. DOI

26. Reske, R.; Mistry, H.; Behafarid, F.; Roldan, C. B.; Strasser, P. Particle size effects in the catalytic electroreduction of CO_2 on Cu nanoparticles. *J. Am. Chem. Soc.* **2014**, *136*, 6978-86. DOI PubMed

27. Kas, R.; Kortlever, R.; Milbrat, A.; Koper, M. T.; Mul, G.; Baltrusaitis, J. Electrochemical CO_2 reduction on Cu_2O-derived copper nanoparticles: controlling the catalytic selectivity of hydrocarbons. *Phys. Chem. Chem. Phys.* **2014**, *16*, 12194-201. DOI PubMed

28. Kuhl, K. P.; Cave, E. R.; Abram, D. N.; Jaramillo, T. F. New insights into the electrochemical reduction of carbon dioxide on metallic copper surfaces. *Energy. Environ. Sci.* **2012**, *5*, 7050-9. DOI

29. Ogura, K.; Oohara, R.; Kudo, Y. Reduction of CO_2 to ethylene at three-phase interface effects of electrode substrate and catalytic coating. *J. Electrochem. Soc.* **2005**, *152*, D213. DOI

30. Han, H.; Han, T.; Luo, Y.; Mushtaq, M. A.; Jia, Y.; Liu, C. Recent advances in α-Fe_2O_3-based photocatalysts for CO_2 conversion to solar fuels. *J. Ind. Eng. Chem.* **2023**, *128*, 81-94. DOI

31. Trogadas, P.; Xu, L.; Coppens, M. O. From biomimicking to bioinspired design of electrocatalysts for CO_2 reduction to C_1 products. *Angew. Chem. Int. Ed.* **2024**, *63*, e202314446. DOI PubMed PMC

32. Wang, Y.; Han, P.; Lv, X.; Zhang, L.; Zheng, G. Defect and interface engineering for aqueous electrocatalytic CO_2 reduction. *Joule* **2018**, *2*, 2551-82. DOI

33. Qiao, J.; Liu, Y.; Hong, F.; Zhang, J. A review of catalysts for the electroreduction of carbon dioxide to produce low-carbon fuels. *Chem. Soc. Rev.* **2014**, *43*, 631-75. DOI

34. Shen, H.; Jin, H.; Li, H.; et al. Acidic CO_2-to-HCOOH electrolysis with industrial-level current on phase engineered tin sulfide. *Nat. Commun.* **2023**, *14*, 2843. DOI PubMed PMC

35. Zhao, K.; Quan, X. Carbon-based materials for electrochemical reduction of CO_2 to C_{2+} oxygenates: recent progress and remaining challenges. *ACS. Catal.* **2021**, *11*, 2076-97. DOI

36. Sun, Z.; Ma, T.; Tao, H.; Fan, Q.; Han, B. Fundamentals and challenges of electrochemical CO_2 reduction using two-dimensional materials. *Chem* **2017**, *3*, 560-87. DOI

37. Woldu, A. R.; Huang, Z.; Zhao, P.; Hu, L.; Astruc, D. Electrochemical CO_2 reduction (CO_2RR) to multi-carbon products over copper-based catalysts. *Coord. Chem. Rev.* **2022**, *454*, 214340. DOI

38. Jiang, K.; Huang, Y.; Zeng, G.; Toma, F. M.; Goddard, W. A.; Bell, A. T. Effects of surface roughness on the electrochemical reduction of CO_2 over Cu. *ACS. Energy. Lett.* **2020**, *5*, 1206-14. DOI

39. Xiao, C.; Zhang, J. Architectural design for enhanced C_2 product selectivity in electrochemical CO_2 reduction using Cu-based catalysts: a review. *ACS. Nano.* **2021**, *15*, 7975-8000. DOI

40. Cho, J. H.; Ma, J.; Kim, S. Y. Toward high-efficiency photovoltaics-assisted electrochemical and photoelectrochemical CO_2 reduction: strategy and challenge. *Exploration* **2023**, *3*, 20230001. DOI PubMed PMC

41. Rhimi, B.; Zhou, M.; Yan, Z.; Cai, X.; Jiang, Z. Cu-based materials for enhanced C_{2+} product selectivity in photo-/electro-catalytic CO_2 reduction: challenges and prospects. *Nano-Micro. Lett.* **2024**, *16*, 64. DOI PubMed PMC

42. Li, D.; Zhang, H.; Xiang, H.; et al. How to go beyond C_1 products with electrochemical reduction of CO_2. *Sustainable. Energy. Fuels.* **2021**, *5*, 5893-914. DOI

43. Garza, A. J.; Bell, A. T.; Head-gordon, M. Mechanism of CO_2 reduction at copper surfaces: pathways to C_2 products. *ACS. Catal.* **2018**, *8*, 1490-9. DOI

44. Lim, C. Y. J.; Yilmaz, M.; Arce-Ramos, J. M.; et al. Surface charge as activity descriptors for electrochemical CO_2 reduction to multi-carbon products on organic-functionalised Cu. *Nat. Commun.* **2023**, *14*, 335. DOI PubMed PMC

45. Calle-Vallejo, F.; Koper, M. T. Theoretical considerations on the electroreduction of CO to C_2 species on Cu(100) electrodes. *Angew. Chem. Int. Ed.* **2013**, *52*, 7282-5. DOI PubMed

46. Ma, M.; Djanashvili, K.; Smith, W. A. Controllable hydrocarbon formation from the electrochemical reduction of CO_2 over Cu nanowire arrays. *Angew. Chem. Int. Ed.* **2016**, *55*, 6680-4. DOI PubMed

47. Wang, L.; Nitopi, S. A.; Bertheussen, E.; et al. Electrochemical carbon monoxide reduction on polycrystalline copper: effects of potential, pressure, and pH on selectivity toward multicarbon and oxygenated products. *ACS. Catal.* **2018**, *8*, 7445-54. DOI

48. Rollier, F. A.; Muravev, V.; Parastaev, A.; et al. Restructuring of Cu-based catalysts during CO electroreduction: evidence for the dominant role of surface defects on the C_{2+} Product Selectivity. *ACS. Catal.* **2024**, *14*, 13246-59. DOI

49. Chang, B.; Pang, H.; Raziq, F. Electrochemical reduction of carbon dioxide to multicarbon (C_{2+}) products: challenges and perspectives. *Energy. Environ. Sci.* **2023**, *16*, 4714-58. DOI

50. Zhang, X.; Guo, S.; Gandionco, K. A.; Bond, A. M.; Zhang, J. Electrocatalytic carbon dioxide reduction: from fundamental principles to catalyst design. *Mater. Today. Adv.* **2020**, *7*, 100074. DOI

51. Ma, J.; Ahn, S. H.; Kim, S. Y. Integration of earth-abundant cocatalysts for high-performance photoelectrochemical energy conversion. *J. Energy. Chem.* **2024**, *88*, 336-55. DOI

52. Meng, Y.; Ding, J.; Liu, Y.; et al. Advancements in amorphous oxides for electrocatalytic carbon dioxide reduction. *Mater. Today. Catal.* **2024**, *7*, 100065. DOI

53. Fan, D.; Zhang, S.; Li, Y.; et al. High selective electrocatalytic reduction of carbon dioxide to ethylene enabled by regulating the microenvironment over Cu-Ag nanowires. *J. Colloid. Interface. Sci.* **2024**, *662*, 786-95. DOI

54. Li, M.; Hu, Y.; Wu, T.; Sumboja, A.; Geng, D. How to enhance the C_2 products selectivity of copper-based catalysts towards electrochemical CO_2 reduction? *Materials. Today.* **2023**, *67*, 320-43. DOI

55. Yu, H.; Wu, H.; Chow, Y. L.; Wang, J.; Zhang, J. Revolutionizing electrochemical CO_2 reduction to deeply reduced products on non-Cu-based electrocatalysts. *Energy. Environ. Sci.* **2024**, *17*, 5336-64. DOI

56. Giulimondi, V.; Mitchell, S.; Pérez-Ramírez, J. Challenges and opportunities in engineering the electronic structure of single-atom catalysts. *ACS. Catal.* **2023**, *13*, 2981-97. DOI PubMed PMC

57. Gu, Z.; Shen, H.; Chen, Z.; et al. Efficient electrocatalytic CO_2 reduction to C_{2+} alcohols at defect-site-rich Cu surface. *Joule* **2021**, *5*, 429-40. DOI

58. Xue, L.; Shi, T.; Han, C.; et al. Boosting hydrocarbon conversion via Cu-doping induced oxygen vacancies on CeO_2 in CO_2 electroreduction. *J. Energy. Chem.* **2025**, *100*, 66-76. DOI

59. Fang, M.; Xia, W.; Han, S.; et al. Boosting CO_2 electroreduction to multi-carbon products via oxygen-rich vacancies and Ce^{4+} -O^{2-} -Cu^+ Structure in Cu/CeO_2 for Stabilizing Cu^+. *ChemCatChem* **2024**, *16*, e202301266. DOI

60. Shen, B.; Jia, T.; Wang, H.; et al. Enhanced electrochemical CO_2 reduction for high ethylene selectivity using iodine-doped copper oxide catalysts. *J. Alloys. and. Compd.* **2024**, *980*, 173550. DOI

61. Jiang, Y.; Choi, C.; Hong, S.; et al. Enhanced electrochemical CO_2 reduction to ethylene over CuO by synergistically tuning oxygen vacancies and metal doping. *Cell. Rep. Phys. Sci.* **2021**, *2*, 100356. DOI

62. Bie, Q.; Yin, H.; Wang, Y.; Su, H.; Peng, Y.; Li, J. Electrocatalytic reduction of CO_2 with enhanced C_2 liquid products activity by the

synergistic effect of Cu single atoms and oxygen vacancies. *Chin. J. Catal.* **2024**, *57*, 96-104. DOI

63. Feng, X.; Jiang, K.; Fan, S.; Kanan, M. W. Grain-boundary-dependent CO_2 electroreduction activity. *J. Am. Chem. Soc.* **2015**, *137*, 4606-9. DOI

64. Bi, X.; Zhao, Y.; Yan, Y.; Wang, H.; Wu, M. Grain boundaries assisting the generation of abundant Cu^+ for highly selective electroreduction of CO_2 to ethanol. *Green. Chem.* **2024**, *26*, 5356-64. DOI

65. Chen, Z.; Wang, T.; Liu, B.; et al. Grain-boundary-rich copper for efficient solar-driven electrochemical CO_2 reduction to ethylene and ethanol. *J. Am. Chem. Soc.* **2020**, *142*, 6878-83. DOI

66. Zhang, Y.; Qi, K.; Lyu, P.; et al. Grain-boundary engineering boosted undercoordinated active sites for scalable conversion of CO_2 to ethylene. *ACS. Nano.* **2024**, *18*, 17483-91. DOI

67. Ding, J.; Song, Q.; Xia, L. Unconventional grain fragmentation creates high-density boundaries for efficient CO_2-to-C_{2+} electro-conversion at ampere-level current density. *Nano. Energy.* **2024**, *128*, 109945. DOI

68. Kong, Y.; Yang, H.; Jia, X.; et al. Constructing favorable microenvironment on copper grain boundaries for CO_2 electro-conversion to multicarbon products. *Nano. Lett.* **2024**, *24*, 9345-52. DOI

69. Wu, W.; Tong, Y.; Chen, P. Regulation strategy of nanostructured engineering on indium-based materials for electrocatalytic conversion of CO_2. *Small* **2024**, *20*, 2305562. DOI

70. Zoubir, O.; Atourki, L.; Ait, A. H.; BaQais, A. Current state of copper-based bimetallic materials for electrochemical CO_2 reduction: a review. *RSC. Adv.* **2022**, *12*, 30056-75. DOI PubMed PMC

71. Liu, G.; Zhan, J.; Zhang, Z.; Zhang, L. H.; Yu, F. Recent advances of the confinement effects boosting electrochemical CO_2 reduction. *Chem. Asian. J.* **2023**, *18*, e202200983. DOI PubMed

72. Kim, J. Y.; Hong, D.; Lee, J. C.; et al. Quasi-graphitic carbon shell-induced Cu confinement promotes electrocatalytic CO_2 reduction toward C_{2+} products. *Nat. Commun.* **2021**, *12*, 3765. DOI PubMed PMC

73. Fan, L.; Geng, Q.; Ma, L.; et al. Evoking C_{2+} production from electrochemical CO_2 reduction by the steric confinement effect of ordered porous Cu_2O. *Chem. Sci.* **2023**, *14*, 13851-9. DOI

74. Liu, L. X.; Cai, Y.; Du, H.; et al. Enriching the local concentration of CO intermediates on Cu cavities for the electrocatalytic reduction of CO_2 to C_{2+} products. *ACS. Appl. Mater. Interfaces.* **2023**, *15*, 16673-9. DOI

75. Pan, Y.; Li, H.; Xiong, J.; et al. Protecting the state of Cu clusters and nanoconfinement engineering over hollow mesoporous carbon spheres for electrocatalytical C-C coupling. *Appl. Catal. B. Environ.* **2022**, *306*, 121111. DOI

76. Liu, C.; Zhang, M.; Li, J.; et al. Nanoconfinement engineering over hollow multi-shell structured copper towards efficient electrocatalytical C-C coupling. *Angew. Chem. Int. Ed.* **2022**, *61*, e202113498. DOI

77. Wu, M.; Zhu, C.; Mao, J.; et al. Dimensional effect of oxide-derived Cu electrocatalysts to reduce CO_2 into multicarbon compounds. *Chem. Eng. J.* **2024**, *499*, 156006. DOI

78. Xie, H.; Xie, R.; Zhang, Z.; et al. Achieving highly selective electrochemical CO_2 reduction to C_2H_4 on Cu nanosheets. *J. Energy. Chem.* **2023**, *79*, 312-20. DOI

79. Wang, P.; Meng, S.; Zhang, B.; et al. Sub-1 nm Cu_2O nanosheets for the electrochemical CO_2 reduction and valence state-activity relationship. *J. Am. Chem. Soc.* **2023**, *145*, 26133-43. DOI

80. Yang, F.; Yang, T.; Li, J.; et al. Boosting the electroreduction of CO_2 to liquid products via nanostructure engineering of Cu_2O catalysts. *J. Catal.* **2024**, *432*, 115458. DOI

81. Gregorio GL, Burdyny T, Loiudice A, Iyengar P, Smith WA, Buonsanti R. Facet-dependent selectivity of Cu catalysts in electrochemical CO_2 reduction at commercially viable current densities. *ACS. Catal.* **2020**, *10*, 4854-62. DOI PubMed PMC

82. Fu, Y.; Xie, Q.; Wu, L.; Luo, J. Crystal facet effect induced by different pretreatment of Cu_2O nanowire electrode for enhanced electrochemical CO_2 reduction to C_{2+} products. *Chin. J. Catal.* **2022**, *43*, 1066-73. DOI

83. Dong, Y.; Ma, X.; Jin, Z.; et al. Full-exposed Cu site of Cu_2O-(100) driven high ethylene selectivity of carbon dioxide reduction. *Appl. Surf. Sci.* **2024**, *653*, 159243. DOI

84. Luo, H.; Li, B.; Ma, J. G.; Cheng, P. Surface modification of nano-Cu_2O for controlling CO_2 electrochemical reduction to ethylene and syngas. *Angew. Chem. Int. Ed.* **2022**, *61*, e202116736. DOI

85. Merino-Garcia, I.; Albo, J.; Irabien, A. Tailoring gas-phase CO_2 electroreduction selectivity to hydrocarbons at Cu nanoparticles. *Nanotechnology* **2018**, *29*, 014001. DOI PubMed

86. Rong, W.; Zou, H.; Zang, W.; et al. Size-dependent activity and selectivity of atomic-level copper nanoclusters during CO/CO_2 electroreduction. *Angew. Chem. Int. Ed.* **2021**, *60*, 466-72. DOI

87. Nam, D. H.; Bushuyev, O. S.; Li, J.; et al. Metal-organic frameworks mediate Cu coordination for selective CO_2 electroreduction. *J. Am. Chem. Soc.* **2018**, *140*, 11378-86. DOI

88. Su, X.; Jiang, Z.; Zhou, J.; et al. Complementary operando spectroscopy identification of in-situ generated metastable charge-asymmetry Cu_2-CuN_3 clusters for CO_2 reduction to ethanol. *Nat. Commun.* **2022**, *13*, 1322. DOI PubMed PMC

89. Tabassum, H.; Yang, X.; Zou, R.; Wu, G. Surface engineering of Cu catalysts for electrochemical reduction of CO_2 to value-added multi-carbon products. *Chem. Catal.* **2022**, *2*, 1561-93. DOI

90. Fang, M.; Wang, M.; Wang, Z.; et al. Hydrophobic, ultrastable $Cu^{\delta+}$ for Robust CO_2 electroreduction to C_2 products at ampere-current levels. *J. Am. Chem. Soc.* **2023**, *145*, 11323-32. DOI

91. Mu, S.; Li, L.; Zhao, R.; Lu, H.; Dong, H.; Cui, C. Molecular-scale insights into electrochemical reduction of CO_2 on hydrophobically modified Cu surfaces. *ACS. Appl. Mater. Interfaces.* **2021**, *13*, 47619-28. DOI

92.   Xie, M. S.; Xia, B. Y.; Li, Y.; et al. Amino acid modified copper electrodes for the enhanced selective electroreduction of carbon dioxide towards hydrocarbons. *Energy. Environ. Sci.* **2016**, *9*, 1687-95. DOI

93.   Wei, X.; Yin, Z.; Lyu, K.; et al. Highly Selective reduction of CO_2 to C_{2+} hydrocarbons at copper/polyaniline interfaces. *ACS. Catal.* **2020**, *10*, 4103-11. DOI

94.   Ma, L.; Geng, Q.; Fan, L.; et al. Enhanced electroreduction of CO_2 to C_{2+} fuels by the synergetic effect of polyaniline/CuO nanosheets hybrids. *Nano. Res.* **2023**, *16*, 9065-72. DOI

95.   Wakerley, D.; Lamaison, S.; Ozanam, F.; et al. Bio-inspired hydrophobicity promotes CO_2 reduction on a Cu surface. *Nat. Mater.* **2019**, *18*, 1222-7. DOI

96.   Shi, T.; Liu, D.; Feng, H.; Zhang, Y.; Li, Q. Evolution of triple-phase interface for enhanced electrochemical CO_2 reduction. *Chem. Eng. J.* **2022**, *431*, 134348. DOI

97.   Niu, Z. Z.; Gao, F. Y.; Zhang, X. L.; et al. Hierarchical copper with inherent hydrophobicity mitigates electrode flooding for high-rate CO_2 electroreduction to multicarbon products. *J. Am. Chem. Soc.* **2021**, *143*, 8011-21. DOI

98.   Liu, Z.; Lv, X.; Kong, S.; et al. Interfacial water tuning by intermolecular spacing for stable CO_2 electroreduction to C_{2+} products. *Angew. Chem. Int. Ed.* **2023**, *62*, e202309319. DOI

99.   Xie, L.; Jiang, Y.; Zhu, W. Cu-based catalyst designs in CO_2 electroreduction: precise modulation of reaction intermediates for high-value chemical generation. *Chem. Sci.* **2023**, *14*, 13629-60. DOI

100. Xie, G.; Guo, W.; Fang, Z.; et al. Dual-metal sites drive tandem electrocatalytic CO_2 to C_{2+} products. *Angew. Chem. Int. Ed.* **2024**, *63*, e202412568. DOI

101. Zhu, C.; Zhang, Z.; Qiao, R.; et al. Selective tandem CO_2-to-C_{2+} alcohol conversion at a single-crystal Au/Cu bimetallic interface. *J. Phys. Chem. C.* **2023**, *127*, 3470-7. DOI

102. Zhang, B.; Wang, L.; Li, D.; Li, Z.; Bu, R.; Lu, Y. Tandem strategy for electrochemical CO_2 reduction reaction. *Chem. Catal.* **2022**, *2*, 3395-429. DOI

103. Zhan, C.; Dattila, F.; Rettenmaier, C.; et al. Key intermediates and Cu active sites for CO_2 electroreduction to ethylene and ethanol. *Nat. Energy.* **2024**, *9*, 1485-96. DOI PubMed PMC

104. Qin, Q.; Suo, H.; Chen, L.; et al. Emerging Cu-Based tandem catalytic systems for CO_2 electroreduction to multi-carbon products. *Adv. Mater. Inter.* **2024**, *11*, 2301049. DOI

105. Duan, H.; Li, W.; Ran, L.; et al. In-situ electrochemical interface of Cu@Ag/C towards the ethylene electrosynthesis with adequate *CO supply. *J. Energy. Chem.* **2024**, *99*, 292-9. DOI

106. Jeon, Y. E.; Ko, Y. N.; Kim, J.; et al. Selective production of ethylene from CO_2 over CuAg tandem electrocatalysts. *J. Ind. Eng. Chem.* **2022**, *116*, 191-8. DOI

107. Liu, H.; Sun, C.; Wu, M.; et al. High-performance carbon dioxide reduction to multi-carbon products on EDTA-modified Cu-Ag tandem catalyst. *J. Catal.* **2024**, *429*, 115227. DOI

108. Luan, P.; Dong, X.; Liu, L.; et al. Selective electrosynthesis of ethanol via asymmetric C-C coupling in tandem CO_2 reduction. *ACS. Catal.* **2024**, *14*, 8776-85. DOI

109. Huang, J.; Mensi, M.; Oveisi, E.; Mantella, V.; Buonsanti, R. Structural sensitivities in bimetallic catalysts for electrochemical CO_2 reduction revealed by Ag-Cu nanodimers. *J. Am. Chem. Soc.* **2019**, *141*, 2490-9. DOI PubMed

110. Ma, Y.; Yu, J.; Sun, M.; et al. Confined growth of silver-copper janus nanostructures with {100} facets for highly selective tandem electrocatalytic carbon dioxide reduction. *Adv. Mater.* **2022**, *34*, e2110607. DOI

111. Wei, C.; Yang, Y.; Ma, H.; et al. Nanoscale management of CO transport in CO_2 electroreduction: boosting faradaic efficiency to multicarbon products via nanostructured tandem electrocatalysts. *Adv. Funct. Mater.* **2023**, *33*, 2214992. DOI

112. Morales-guio, C. G.; Cave, E. R.; Nitopi, S. A.; et al. Improved CO_2 reduction activity towards C_{2+} alcohols on a tandem gold on copper electrocatalyst. *Nat. Catal.* **2018**, *1*, 764-71. DOI

113. Wang, S.; Jung, H. D.; Choi, H.; Kim, J.; Back, S.; Oh, J. Delicate control of a gold-copper oxide tandem structure enables the efficient production of high-value chemicals by electrochemical carbon dioxide reduction. *Nano. Energy.* **2024**, *130*, 110176. DOI

114. Cao, X.; Cao, G.; Li, M.; et al. Enhanced ethylene formation from carbon dioxide reduction through sequential catalysis on Au decorated cubic Cu_2O electrocatalyst. *Eur. J. Inorg. Chem.* **2021**, *2021*, 2353-64. DOI

115. Zhu, C.; Zhou, L.; Zhang, Z.; et al. Dynamic restructuring of epitaxial Au-Cu biphasic interface for tandem CO_2-to-C_{2+} alcohol conversion. *Chem* **2022**, *8*, 3288-301. DOI

116. Wei, Z.; Yue, S.; Gao, S.; Cao, M.; Cao, R. Synergetic effects of gold-doped copper nanowires with low Au content for enhanced electrocatalytic CO_2 reduction to multicarbon products. *Nano. Res.* **2023**, *16*, 7777-83. DOI

117. Zheng, Y.; Zhang, J.; Ma, Z.; et al. Seeded growth of gold-copper janus nanostructures as a tandem catalyst for efficient electroreduction of CO_2 to C_{2+} products. *Small* **2022**, *18*, e2201695. DOI

118. Huang, J.; Zhang, X.; Yang, J.; Yu, J.; Chen, Q.; Peng, L. Recent progress on copper-based bimetallic heterojunction catalysts for CO_2 electrocatalysis: unlocking the mystery of product selectivity. *Adv. Sci.* **2024**, *11*, 2309865. DOI

119. Li, Y.; Sun, Y.; Yu, M. Strategies for improving product selectivity in electrocatalytic carbon dioxide reduction using copper-based catalysts. *Adv. Funct. Mater.* **2024**, *34*, 2410186. DOI

120. Wan, L.; Zhang, X.; Cheng, J.; et al. Bimetallic Cu-Zn catalysts for electrochemical CO_2 reduction: phase-separated versus core-shell distribution. *ACS. Catal.* **2022**, *12*, 2741-8. DOI

121. Liu, J.; Yu, K.; Qiao, Z.; Zhu, Q.; Zhang, H.; Jiang, J. Integration of cobalt phthalocyanine, acetylene black and Cu_2O nanocubes for

efficient electroreduction of CO_2 to C_2H_4. *ChemSusChem* **2023**, *16*, e202300601. DOI

122. Kong, X.; Zhao, J.; Ke, J.; et al. Understanding the effect of *CO coverage on C-C coupling toward CO_2 electroreduction. *Nano. Lett.* **2022**, *22*, 3801-8. DOI

123. Min, S.; Xu, X.; He, J.; Sun, M.; Lin, W.; Kang, L. Construction of cobalt porphyrin-modified Cu_2O nanowire array as a tandem electrocatalyst for enhanced CO_2 reduction to C_2 products. *Small* **2024**, *20*, 2400592. DOI

124. Chen, Y.; Ji, S.; Chen, C.; Peng, Q.; Wang, D.; Li, Y. Single-atom catalysts: synthetic strategies and electrochemical applications. *Joule* **2018**, *2*, 1242-64. DOI

125. Zhang, L.; Wang, K.; Zhu, G.; Shi, J.; Zhu, H. Assembly of colloidal Cu nanoparticles and Ni-N-C nanocarbons to electrochemically boost cascade production of ethylene from CO_2 reduction. *J. Mater. Sci.* **2023**, *58*, 17200-10. DOI

126. Zhang, Y.; Li, P.; Zhao, C.; et al. Multicarbons generation factory: CuO/Ni single atoms tandem catalyst for boosting the productivity of CO_2 electrocatalysis. *Sci. Bull.* **2022**, *67*, 1679-87. DOI

127. Liu, M.; Wang, Q.; Luo, T.; et al. Potential alignment in tandem catalysts enhances CO_2-to-C_2H_4 conversion efficiencies. *J. Am. Chem. Soc.* **2024**, *146*, 468-75. DOI

128. Meng, D. L.; Zhang, M. D.; Si, D. H.; et al. Highly selective tandem electroreduction of CO_2 to ethylene over atomically isolated nickel-nitrogen site/copper nanoparticle catalysts. *Angew. Chem. Int. Ed.* **2021**, *60*, 25689-96. DOI

129. Chen, B.; Gong, L.; Li, N.; et al. Tandem catalysis for enhanced CO_2 to ethylene conversion in neutral media. *Adv. Funct. Mater.* **2024**, *34*, 2310029. DOI

130. Paris, A. R.; Bocarsly, A. B. Ni-Al films on glassy carbon electrodes generate an array of oxygenated organics from CO_2. *ACS. Catal.* **2017**, *7*, 6815-20. DOI

131. Torelli, D. A.; Francis, S. A.; Crompton, J. C.; et al. Nickel-gallium-catalyzed electrochemical reduction of CO_2 to highly reduced products at low overpotentials. *ACS. Catal.* **2016**, *6*, 2100-4. DOI

132. Ding, J.; Bin, Y. H.; Ma, X.; et al. A tin-based tandem electrocatalyst for CO_2 reduction to ethanol with 80% selectivity. *Nat. Energy.* **2023**, *8*, 1386-94. DOI

133. She, X.; Wang, Y.; Xu, H.; Chi, E. T. S.; Ping, L. S. Challenges and opportunities in electrocatalytic CO_2 reduction to chemicals and fuels. *Angew. Chem. Int. Ed.* **2022**, *61*, e202211396. DOI

134. Ewis, D.; Arsalan, M.; Khaled, M.; et al. Electrochemical reduction of CO_2 into formate/formic acid: A review of cell design and operation. *Sep. Purif. Technol.* **2023**, *316*, 123811. DOI

135. Harthi A, Abri MA, Younus HA, Hajri RA. Criteria and cutting-edge catalysts for CO_2 electrochemical reduction at the industrial scale. *J. CO2. Util.* **2024**, *83*, 102819. DOI

136. Sajna, M.; Zavahir, S.; Popelka, A.; et al. Electrochemical system design for CO_2 conversion: a comprehensive review. *J. Environ. Chem. Eng.* **2023**, *11*, 110467. DOI

137. Kim, J.; Ahn, S. H. Recent progress in carbon dioxide electrolyzer using gas diffusion electrode. *Ceramist* **2021**, *24*, 96-108. DOI

138. Luo, Y.; Zhang, K.; Li, Y.; Wang, Y. Valorizing carbon dioxide via electrochemical reduction on gas-diffusion electrodes. *InfoMat* **2021**, *3*, 1313-32. DOI

139. Zhang, F. Y.; Sheng, T.; Tian, N.; et al. Cu overlayers on tetrahexahedral Pd nanocrystals with high-index facets for CO_2 electroreduction to alcohols. *Chem. Commun.* **2017**, *53*, 8085-8. DOI

140. Salvatore, D.; Berlinguette, C. P. Voltage matters when reducing CO_2 in an electrochemical flow cell. *ACS. Energy. Lett.* **2020**, *5*, 215-20. DOI

141. Chen, J.; Qiu, H.; Zhao, Y.; et al. Selective and stable CO_2 electroreduction at high rates via control of local H_2O/CO_2 ratio. *Nat. Commun.* **2024**, *15*, 5893. DOI PubMed PMC

142. Lee, G.; Rasouli, A. S.; Lee, B.; et al. CO_2 electroreduction to multicarbon products from carbonate capture liquid. *Joule* **2023**, *7*, 1277-88. DOI

143. Ni, W.; Chen, H.; Tang, N.; et al. High-purity ethylene production via indirect carbon dioxide electrochemical reduction. *Nat. Commun.* **2024**, *15*, 6078. DOI PubMed PMC

144. Weekes, D. M.; Salvatore, D. A.; Reyes, A.; Huang, A.; Berlinguette, C. P. Electrolytic CO_2 reduction in a flow cell. *Acc. Chem. Res.* **2018**, *51*, 910-8. DOI

145. Sato, S.; Sekizawa, K.; Shirai, S.; Sakamoto, N.; Morikawa, T. Enhanced performance of molecular electrocatalysts for CO_2 reduction in a flow cell following K^+ addition. *Sci. Adv.* **2023**, *9*, eadh9986. DOI

146. Ampelli, C.; Tavella, F.; Giusi, D.; Ronsisvalle, A. M.; Perathoner, S.; Centi, G. Electrode and cell design for CO_2 reduction: a viewpoint. *Catal. Today.* **2023**, *421*, 114217. DOI

147. Tufa, R. A.; Chanda, D.; Ma, M.; et al. Towards highly efficient electrochemical CO_2 reduction: cell designs, membranes and electrocatalysts. *Appl. Energy.* **2020**, *277*, 115557. DOI

148. Xing, Z.; Hu, L.; Ripatti, D. S.; Hu, X.; Feng, X. Enhancing carbon dioxide gas-diffusion electrolysis by creating a hydrophobic catalyst microenvironment. *Nat. Commun.* **2021**, *12*, 136. DOI PubMed PMC

149. Yang, K.; Kas, R.; Smith, W. A.; Burdyny, T. Role of the carbon-based gas diffusion layer on flooding in a gas diffusion electrode cell for electrochemical CO_2 reduction. *ACS. Energy. Lett.* **2021**, *6*, 33-40. DOI

150. Jiang, H.; Luo, R.; Li, Y.; Chen, W. Recent advances in solid-liquid-gas three-phase interfaces in electrocatalysis for energy conversion and storage. *EcoMat* **2022**, *4*, e12199. DOI

151. Wang, J.; Ji, Q.; Zang, H.; et al. Atomically dispersed ga synergy lewis acid-base pairs in F-doped mesoporous Cu_2O for efficient

eletroreduction of CO_2 to C_{2+} products. *Adv. Funct. Mater.* **2024**, *34*, 2404274. DOI

152. Yang, C.; Wang, R.; Yu, C.; et al. Engineering stable Cu^+-Cu^0 sites and oxygen defects in boron-doped copper oxide for electrocatalytic reduction of CO_2 to C_{2+} products. *Chem. Eng. J.* **2024**, *484*, 149710. DOI

153. Chen, Q.; Wang, X.; Zhou, Y.; et al. Electrocatalytic CO_2 reduction to C_{2+} products in flow cells. *Adv. Mater.* **2024**, *36*, 2303902. DOI

154. Yu, J.; Xiao, J.; Ma, Y.; et al. Acidic conditions for efficient carbon dioxide electroreduction in flow and MEA cells. *Chem. Catal.* **2023**, *3*, 100670. DOI

155. Wang, B.; Song, L.; Peng, C.; Lv, X.; Zheng, G. Pd-induced polarized Cu^0-Cu^+ sites for electrocatalytic CO_2-to-C_{2+} conversion in acidic medium. *J. Colloid. Interface. Sci.* **2024**, *671*, 184-91. DOI

156. Wang, Z.; Zhou, Y.; Qiu, P.; et al. Advanced catalyst design and reactor configuration upgrade in electrochemical carbon dioxide conversion. *Adv. Mater.* **2023**, *35*, 2303052. DOI

157. Choi, W.; Park, S.; Jung, W.; Won, D. H.; Na, J.; Hwang, Y. J. Origin of hydrogen incorporated into ethylene during electrochemical CO_2 reduction in membrane electrode assembly. *ACS. Energy. Lett.* **2022**, *7*, 939-45. DOI

158. Rabiee, H.; Ma, B.; Yang, Y.; et al. Advances and challenges of carbon-free gas-diffusion electrodes (GDEs) for electrochemical CO_2 reduction. *Adv. Funct. Mater.* **2025**, *35*, 2411195. DOI

159. Ge, L.; Rabiee, H.; Li, M.; et al. Electrochemical CO_2 reduction in membrane-electrode assemblies. *Chem* **2022**, *8*, 663-92. DOI

160. Gawel, A.; Jaster, T.; Siegmund, D.; et al. Electrochemical CO_2 reduction - the macroscopic world of electrode design, reactor concepts & economic aspects. *iScience* **2022**, *25*, 104011. DOI

161. Lee, T.; Lee, Y.; Eo, J.; Nam, D. H. Acidic CO_2 electroreduction for high CO_2 utilization: catalysts, electrodes, and electrolyzers. *Nanoscale* **2024**, *16*, 2235-49. DOI

162. Alinejad, S.; Quinson, J.; Li, Y.; et al. Optimizing the use of a gas diffusion electrode setup for CO_2 electrolysis imitating a zero-gap MEA design. *J. Catal.* **2024**, *429*, 115209. DOI

163. Larrea, C.; Torres, D.; Avilés-moreno, J. R.; Ocón, P. Multi-parameter study of CO_2 electrochemical reduction from concentrated bicarbonate feed. *J. CO2. Util.* **2022**, *57*, 101878. DOI

164. Bui, J. C.; Kim, C.; King, A. J.; et al. Engineering catalyst-electrolyte microenvironments to optimize the activity and selectivity for the electrochemical reduction of CO_2 on Cu and Ag. *Acc. Chem. Res.* **2022**, *55*, 484-94. DOI

165. Lai, W.; Qiao, Y.; Zhang, J.; Lin, Z.; Huang, H. Design strategies for markedly enhancing energy efficiency in the electrocatalytic CO_2 reduction reaction. *Energy. Environ. Sci.* **2022**, *15*, 3603-29. DOI

166. Ozden, A.; Li, F.; García, A. F. P.; et al. High-rate and efficient ethylene electrosynthesis using a catalyst/promoter/transport layer. *ACS. Energy. Lett.* **2020**, *5*, 2811-8. DOI

167. He, R.; Xu, N.; Hasan, I. M. U.; et al. Advances in electrolyzer design and development for electrochemical CO_2 reduction. *EcoMat* **2023**, *5*, e12346. DOI

168. Xia, C.; Zhu, P.; Jiang, Q.; et al. Continuous production of pure liquid fuel solutions via electrocatalytic CO_2 reduction using solid-electrolyte devices. *Nat. Energy.* **2019**, *4*, 776-85. DOI

169. Gong, Y.; He, T. Gaining deep understanding of electrochemical CO_2RR with in situ/operando techniques. *Small. Methods.* **2023**, *7*, 2300702. DOI

170. Delmo, E. P.; Wang, Y.; Song, Y.; et al. *In situ* infrared spectroscopic evidence of enhanced electrochemical CO_2 reduction and C-C coupling on oxide-derived copper. *J. Am. Chem. Soc.* **2024**, *146*, 1935-45. DOI

171. Xu, H.; Fan, Z.; Zhu, S.; Shao, M. A minireview on selected applications of in situ infrared spectroscopy in studying CO_2 electrochemical reduction reaction. *Curr. Opin. Electrochem.* **2023**, *41*, 101363. DOI

172. Chen, L.; Zhang, C.; Jiao, X. Recent advances of in situ insights into CO_2 reduction toward fuels. *ChemCatChem* **2025**, *17*, e202401388. DOI

173. Jin, L.; Seifitokaldani, A. In situ spectroscopic methods for electrocatalytic CO_2 reduction. *Catalysts* **2020**, *10*, 481. DOI

174. Katayama, Y.; Nattino, F.; Giordano, L.; et al. An *in situ* surface-enhanced infrared absorption spectroscopy study of electrochemical CO_2 reduction: selectivity dependence on surface C-bound and O-bound reaction intermediates. *J. Phys. Chem. C.* **2019**, *123*, 5951-63. DOI

175. Dutta, A.; Kuzume, A.; Rahaman, M.; Vesztergom, S.; Broekmann, P. Monitoring the chemical state of catalysts for CO_2 electroreduction: an in operando study. *ACS. Catal.* **2015**, *5*, 7498-502. DOI

176. Zhu, P.; Qin, Y.; Cai, X.; et al. Understanding oxidation state of Cu-based catalysts for electrocatalytic CO_2 reduction. *J. Mater. Sci. Technol.* **2025**, *218*, 1-24. DOI

177. Firet, N. J.; Smith, W. A. Probing the reaction mechanism of CO_2 electroreduction over Ag films via operando infrared spectroscopy. *ACS. Catal.* **2017**, *7*, 606-12. DOI

178. Chen, M.; Liu, D.; Qiao, L.; et al. In-situ/operando raman techniques for in-depth understanding on electrocatalysis. *Chem. Eng. J.* **2023**, *461*, 141939. DOI

179. Celorrio, V.; Leach, A. S.; Huang, H.; et al. Relationship between Mn oxidation state changes and oxygen reduction activity in $(La,Ca)MnO_3$ as probed by *in situ* XAS and XES. *ACS. Catal.* **2021**, *11*, 6431-9. DOI

180. Song, X.; Xu, L.; Sun, X.; Han, B. In situ/operando characterization techniques for electrochemical CO_2 reduction. *Sci. China. Chem.* **2023**, *66*, 315-23. DOI

181. You, S.; Xiao, J.; Liang, S.; et al. Doping engineering of Cu-based catalysts for electrocatalytic CO_2 reduction to multi-carbon

products. *Energy. Environ. Sci.* **2024**, *17*, 5795-818. DOI

182. Popović, S.; Smiljanić, M.; Jovanovič, P.; Vavra, J.; Buonsanti, R.; Hodnik, N. Stability and degradation mechanisms of copper-based catalysts for electrochemical CO_2 reduction. *Angew. Chem. Int. Ed.* **2020**, *59*, 14736-46. DOI PubMed

183. He, Q.; Ning, J.; Chen, H.; et al. Achievements, challenges, and perspectives in the design of polymer binders for advanced lithium-ion batteries. *Chem. Soc. Rev.* **2024**, *53*, 7091-157. DOI